Tungsten mineralization during evolution of a magmatic–hydrothermal system: mineralogical evidence from the Xihuashan rare-metal granite in South China

Revision 2

JIE LI [1, 2], XIAO-LONG HUANG [1, *], QI FU [3], WU-XIAN LI [1]

[1] *State Key Laboratory of Isotope Geochemistry, Guangzhou Institute of Geochemistry, Chinese Academy of Sciences, Guangzhou 510640, China*

[2] *Key Laboratory of Submarine Geosciences, Second Institute of Oceanography, Ministry of Natural Resources, Hangzhou 310012, China*

[3] *Department of Earth and Atmospheric Sciences, University of Houston, Houston, TX 77204-5007, USA*

* Corresponding author: Xiao-Long Huang (e-mail: xlhuang@gig.ac.cn; Tel: +86-20-85290010; ORCID: 0000-0002-3138-986X)

ABSTRACT

Tungsten deposits are usually associated with granitic intrusions that record a long and complex evolution of the magmatic–hydrothermal system. However, the genetic link between magmatic–hydrothermal evolution and tungsten mineralization remains unclear. The Xihuashan tungsten deposit in South China, an important vein-type wolframite deposit, is closely associated with greisen and multiphase intrusive activity that produced biotite granite, two-mica granite, and muscovite granite. From the biotite granite to the two-mica granite to the muscovite granite, micas vary from siderophyllite to lithian siderophyllite, with decreasing K/Rb and Nb/Ta ratios and increasing Rb and Cs contents. The zoned micas in the muscovite granite and greisen display fluorine-depleted rims, reflecting subsolidus replacement by external aqueous fluids. The presence of siderite indicates a Fe, Mn and CO_2-rich fluid under reducing conditions. The micas in the greisen have higher F contents and lower Fe^{3+}/Fe^{2+} ratios than those in the muscovite granite, suggesting that the fluids contributing to greisen formation had a relatively high fluorine content and were reduced. The increase of CO_2 in the fluid enhanced its ability to unlock W from melts/rocks into fluids. The reducing environment also facilitated the tungsten mineralization. During greisenization, the pH value of the fluid increased, which destabilized the polymeric tungstates to form WO_4^{2-}. The mixture of W-rich solution and Fe, Mn-rich external fluid eventually precipitated as vein-type wolframite in favorable locations. An empirical equation ($Li_2O = 0.0748 \times F^2 + 0.0893 \times F$) was introduced for estimating the Li_2O contents of hydrothermal micas using the F contents determined by EPMA.

Key words: rare-metal granite; tungsten mineralization; magmatic–hydrothermal evolution; mica; siderite; South China

INTRODUCTION

Most tungsten deposits are closely associated with granitic intrusions, and the styles of mineralization may be diverse, including quartz veins, stockworks, breccia, skarn, greisen, pegmatite, and porphyry. Wolframite-bearing quartz veins, regarded as an important type of hydrothermal deposit, commonly occur in differentiated granitic plutons that show varying degrees of hydrothermal alteration (e.g., Gleeson et al. 2001; Schaltegger et al. 2005; Vigneresse 2006). The relationship between magmatic–hydrothermal activities and tungsten mineralization is therefore a critical issue in understanding the formation of tungsten deposits. For individual deposits, the role of the intrusion as the main source of fluids and metals is usually unclear due to the multiple overprint/reopening of the veins and to the lack of geochronological data constraining the timing of magmatic and hydrothermal events. It has been proposed that the ore-forming elements may be concentrated during multiple stages of magmatic activity and then extracted by magmatic fluids (e.g., Che et al. 2013; Harlaux et al. 2018a), or be leached from granitoids and/or metamorphic rocks and transported by external (metamorphic or meteoric) fluids (e.g., Linnen and Williams–Jones et al. 1995; Vindel et al. 1995; Vallance et al. 2001). Most previous studies on the relationship between magmatic–hydrothermal episodes and tungsten mineralization have been based on the geochronology of deposits and their host granites (e.g., Wang et al. 2011; Li et al. 2013), experiments on partition coefficients between minerals and fluids/melts (e.g., Linnen and Cuney 2005; Che et al. 2013), analyses of fluid inclusions (e.g., Wei et al. 2012), and analyses of mineral geochemistry and stable isotopes (Legros et al. 2019). Although recent studies have successfully dated wolframite from tungsten deposits (e.g., Harlaux et al. 2018b; Deng et al. 2019), limitations still exist, owing to the lack of suitable techniques for precisely dating both hydrothermal deposits and associated granitoids, the intrinsic differences between modeled and natural granitic systems, and uncertainties on whether fluid inclusions are representative of ore-forming fluids.

The textures and chemical compositions of ore-bearing oxide minerals, rock-forming minerals, and even accessory minerals may be used to track magmatic–hydrothermal processes in granitic systems and related metal mineralization (e.g., Roda–Robles et al. 2007; Van Lichtervelde et al. 2008; Yang et al. 2013; Li et al. 2015; Yin et al. 2019). Micas are ubiquitous minerals in peraluminous granitic systems, and these primary magmatic or secondary minerals (due to fluid interactions) have the potential to record the processes of fractional crystallization and hydrothermal evolution. As the major rock-forming mineral that hosts tungsten (e.g., 1.9−198 ppm in micas from peraluminous granites; Simons et al. 2017; El Korh et al. 2020), micas provide an effective proxy for tracing the progressive enrichment and ore-forming processes during magmatic–hydrothermal evolution (Legros et al. 2016, 2018; Yin et al. 2019). In addition to CO_2-rich fluid inclusions, carbonates (including synchysite, siderite, and calcite) may occur frequently in rocks associated with tungsten deposits, suggesting that the fluids involved in W-mineralization are enriched in CO_2 (Castorina and Masi 2008; Wei et al. 2012).

The widespread rare-metal deposits in South China are closely associated with Mesozoic granitic rocks, and an example is the Nanling W–Sn polymetallic mineralization region (Fig. 1a) (Yin et al. 1995; Wang et al. 2003; Li et al. 2015). The Xihuashan tungsten deposit located in the Jiangxi Province is a typical vein-type wolframite deposit with minor Sn–Be mineralization (Nie and Wang 2007), and it is one of the major tungsten deposits in the world (Sinclair et al. 2014). The Xihuashan deposit is spatially and temporally associated with Jurassic granitic intrusions (Wang et al. 2011; Li et al. 2013; Yang et al. 2018), and it shows genetic links with the magmatic and hydrothermal evolution of the granitic intrusions. This deposit therefore provides an opportunity to investigate the mechanism of W enrichment and mineralization in rare-metal granites during the evolution of the magmatic–hydrothermal system. Previous studies on the Xihuashan deposit were focused mainly on the geochronology of the deposits and related granites (Wang et al. 2011; Guo et al. 2012; Hu et al. 2012; Li et al. 2013), fluid inclusions and wolframite formation (Wei et al. 2012; Huang et al. 2013), and magmatic fractionation or hydrothermal alteration of the granites (Le Bel et al. 1983; Maruéjol et al. 1990; Wang et al. 2003; Yang et al. 2013). This paper presents the results of whole-rock major and trace element analyses of the Xihuashan rare-metal granite as well as the chemical compositions of the micas and siderite, to elucidate the relationships between the tungsten mineralization and the magmatic–hydrothermal evolution of highly fractionated granitic melts, and to reveal the relative contributions of magmatic and hydrothermal processes to the formation of tungsten ore deposits. The results show the critical role of greisenizing fluids and magma fractionation in the tungsten mineralization, and provide new insights into the metallogenesis of tungsten in rare-metal granites.

GEOLOGICAL SETTING AND PETROGRAPHY

The South China Block (SCB) comprises the Yangtze Block in the northwest and the Cathaysia Block in the southeast (Fig. 1a). The two blocks were amalgamated during the early Neoproterozoic (e.g., Li et al. 2009; Zhao et al. 2011). During the Phanerozoic, the Cathaysia Block was subjected to intensive and widespread multiphase orogenesis and magmatism (Li et al. 2012). The igneous rocks of Jurassic and Cretaceous age are predominantly granites and rhyolites with subordinate mafic and rare intermediate lithologies (Zhou et al. 2006; Li et al. 2012). The Jurassic rocks occur over large parts of the Cathaysia Block, while the Cretaceous rocks cover the coastal area of SE China and the middle to lower reaches of the Yangtze River in the Yangtze Block (Fig. 1a). The majority of highly evolved and peraluminous granitic rocks were formed during the Jurassic with a few during the Cretaceous (Legros et al. 2020). These rocks in the Nanling area are associated with W–Sn–Mo–Bi–Be–Nb–Ta mineralization, and the area is well known as the Nanling tungsten–tin polymetallic mineralization region (NPMR, Fig. 1a) (e.g., Wang et al. 1982; Pei and Hong 1995).

The Xihuashan mining district is located in the southwestern part of the Jiangxi Province, South China (Fig. 1). It contains more than 700 economically viable ore veins, including W–Sn–Be mineralization (Nie and Wang 2007). There are six main tungsten mines in the district, namely Xihuashan, Dangping, Shenlongkou, Luokeng, Xialuogushan, and Niuzishi (Fig. 1b). The Xihuashan Mine hosts the largest vein-type wolframite deposit in the district, with the total estimate of WO_3 being 81,300 tons and an average ore grade of 1.08 % WO_3 (Wei et al. 2012). The deposit is spatially and temporally related to a multiphase granitic intrusion that crops out over an area of about 20 km^2 (Guo et al. 2012). Previous geochronological studies indicated a close temporal relationship between the granitic magmatism and the W mineralization. For example, the crystallization ages of the major intrusions are 156–161 Ma (Guo et al. 2012; Li et al. 2013; Tang et al. 2020), and the Re–Os ages of molybdenites in the ore are identical (157 ± 3 Ma; Wang et al. 2011). The Xihuashan granitic complex was emplaced in upper Cambrian low-grade metamorphosed flysch-like sedimentary rocks, which underwent contact metamorphism (Le Bel et al. 1984). Wei et al. (2012) suggested the ore-forming fluids to be a mixture of magmatic and hydrothermal fluids derived from the granitic melts and meteoric water. With the knowledge obtained from geological mapping and exploratory drilling, the Xihuashan granitic complex may be divided into four successive intrusions (G1–G4; Fig. 1b) (Maruéjol et al. 1990; Wang et al. 2003). The G1 (coarse-grained biotite granite) occurs as the outermost part of the complex. The G2 (medium-grained biotite granite) hosts tungsten mineralization at the Xihuashan Mine. The G3 (medium- to fine-grained biotite granite) hosts tungsten mineralization at the Dangping Mine, whereas the G4 (fine-grained biotite granite) occurs as a barren border of G3.

The collected samples of G2 (medium-grained biotite granite) in the Xihuashan Mine include biotite granite, two-mica (lithian siderophyllite–muscovite) granite, muscovite granite, and greisen (Fig. 2a–d). The biotite granite crops out over an area of about 5.2 km^2. The greisen, two-mica granite and muscovite granite are only exposed in the sub-surface and were investigated using drilled samples and exposure in the mine tunnels. Liu (2005) and Huang et al. (2006) showed that the greisen was usually associated with tungsten ore veins cutting the fine-grained two-mica granite, the muscovite granite, or the country rocks. There is a transition between the two-mica granite and the muscovite granite, both of which intruded the biotite granite (Liu 2005; Huang et al. 2006). The main accessory minerals of the Xihuashan intrusive rocks are fluorite, apatite, zircon, thorite, xenotime, and rutile (Supplementary Table 1).

The *biotite granite* consists of quartz (32–38%), K-feldspar (19–20%), plagioclase (32–34%), and siderophyllite (8–13%) (Fig. 2a). Plagioclase is subhedral or euhedral and shows compositional zoning. The siderophyllite grains are coarse and up to 2 mm in diameter. The plagioclase and siderophyllite alway host inclusions of ilmenite and apatite. Rutile is common as a secondary mineral associated with chloritization of the micas. The fluorite grains are anhedral and contain high yttrium contents (Y_2O_3 = 8–15 wt%). The accessory minerals enriched in REEs include apatite, monazite, allanite, and zircon.

The *two-mica (lithian siderophyllite–muscovite) granite* is composed mainly of quartz (30–35%), K-feldspar (14–15%), plagioclase (43–49%), and micas (6–8%) (Fig. 2b). The micas are dominantly lithian siderophyllite (~6%) with lesser amounts of muscovite (~2%). The primary mica crystals are coarse and up to 2 mm in size, while most secondary micas are fine-grained sericite within large plagioclase and K-feldspar phenocrysts. The lithian siderophyllite always contains inclusions of ilmenite and apatite, and the rims always show porosity due to dissolution. Xenotime is the principal phosphate mineral in the two-mica granite, and other common accessory minerals are zircon, garnet, and fluorite.

The *muscovite granite* consists of quartz (39–45%), K-feldspar (19–22%), plagioclase (32–35%), and muscovite (~4%) (Fig. 2c). The accessory minerals include spessartine, zircon, fluorite, xenotime, and siderite. The siderite crystals are anhedral and elongate, and they occur mostly along the cleavages of the micas.

The *greisen* is composed of quartz (49–55%), lithian siderophyllite (30–35%), and muscovite (9–11%) (Fig. 2d). The principal accessory minerals include zircon, xenotime, fluorite, siderite, niobotantalates, and wolframite. Xenotime and zircon are the predominant REE-rich minerals, while niobotantalates and wolframite are the tungsten-bearing minerals.

ANALYTICAL METHODS

The whole rock geochemical analyses were carried out at the State Key Laboratory of Isotope Geochemistry (SKLaBIG), Guangzhou Institute of Geochemistry (GIG), Chinese Academy of Sciences (CAS). To eliminate potential contamination, samples were cut into slabs and the central parts (> 200 g) were selected for whole-rock analyses. The rocks were crushed into pieces with size of < 0.5 cm in diameter, cleaned with deionized water in ultrasonic bath, and then pulverized in a corundum mill. Major element oxides were determined using a Rigaku RIX 2000 X-ray fluorescence (XRF) spectrometer. Samples were prepared as glass discs by a Rigaku desktop fusion machine, mixing 0.50 g of rock powder (dried at 110 °C) with 4.0 g of $Li_2B_4O_7$ for 15 min at

1100 °C in 95% Pt - 5% Au crucibles. Calibration lines used for quantification were produced by bivariate regression of data from 36 reference materials. Matrix corrections were also incorporated into calibration using the empirical Traill-Lachance procedure. For whole rock analyses, total Fe is reported as Fe_2O_3 (Supplementary Table 2). The analytical uncertainty was between 1 % and 5 %. The additional quantitative analysis of F was conducted by ALS Chemex (Guangzhou) Co Ltd., China, using the methods of KOH fusion and ion selective electrode, or Na_2O_2 fusion, citric acid leach and ion selective electrode. Analytical precision of F was lower than 10%.

Trace elements were determined using inductively coupled plasma-mass spectrometry (ICP-MS). The rock powder was digested in a mixture of HF and HNO_3 in high-pressure Teflon bombs. An internal standard solution containing single element Rh was used to monitor signal drift. The detailed procedure was described in Li et al. (2006). The US Geological Survey and Chinese National Standards, including SARM-4, W-2, BHVO-2, AGV-2, GSR-1, GSR-2 and GSR-3, were used for calibration. Analytical precision of REE and other incompatible elements was in the range of 1 to 5 %.

The siderites were examined using HORIBA Xplora laser Raman microspectroscopy at the Key Laboratory of Mineralogy and Metallogeny (KLMM), GIG-CAS. An Ar ion laser operated at 44 mW was used to produce an excitation line with wavelength of 532 nm. The scanning range of spectra was set between 100 and 4000 cm^{-1} with an accumulation time of 10 s for each scan. The spectral resolution was 0.65 cm^{-1}. The Raman shift of a monocrystalline silicon piece was measured to be 520.7

cm^{-1} before analyses.

Back-scattered-electron (BSE) images were obtained by a Zeiss Supra 55 field-emission scanning electron microscope (FE-SEM) at the SKLaBIG-GIG-CAS. The *in-situ* mineral composition analyses were performed using the JEOL JXA8100 electron probe micro-analyzer (EPMA) at the SKLaBIG-GIG-CAS, with the operating conditions of 15 kV accelerating voltage, 20 nA beam current and 1 μm beam size (siderite) or 5 μm beam size (micas). A variable peak counting time of 7–40 s was designed for the intensity of the characteristic X-ray lines and desired precision (Supplementary Table 3). The raw data were corrected using ZAF correction. For micas, the detection limits for most elements are lower than 251 ppm, and those for F and Rb are 568 ppm and 631 ppm, respectively (Supplementary Table 3). Relative uncertainties were estimated to be ca. 7% for F and 10–15 % (1σ) for Cl. Chemical formulae of micas were calculated from mineral analyses based on 24 anions (O, F, OH), and Fe^{3+} was estimated following the method by Lin and Peng (1994) described in Supplementary Table 4. The CO_2 content in siderite was calculated by stoichiometry.

In-situ trace element concentrations were measured in mica and siderite grains using an Agilent 7500a quadrupole ICP-MS coupled with a RESOlution M-50 laser ablation system at the KLMM-GIG-CAS. The operating conditions included a spot size of 42 μm, repetition rate of 5 Hz, maximum energy of 90 mJ and laser fluence of 7 J/cm^2. Argon was used as a make-up gas and mixed with helium as the carrier gas via a cyclone mixer prior to entering the ICP torch. The National Institute of Standards and Technology (NIST) 610 glass and 612 glass were used as external standards for quality control (Jochum et al. 2011). Every analysis of six samples was followed by NIST 610 and 612 standards for time-dependent calibration of sensitivity drift. The internal standards are ^{27}Al and ^{57}Fe for mica and siderite, respectively. The off-line data processing was performed using the commercial software ICPMSDataCal 6.7 (Liu et al. 2008). The dwell time of each spot is 70 s of analysis time (30 s background, 40 s ablation). Limits of detection (LOD) were calculated using the 3σ criterion detailed by Longerich et al. (1996). The relative standard deviation (RSD) varies from 1% to 10%. More details on the standards are reported in Supplementary Table 5.

WHOLE-ROCK COMPOSITIONS

Eight samples (two of each rock type) were analyzed for their whole rock major and trace element compositions (Supplementary Table 2). The granite samples are all peraluminous (A/CNK = 1.02–1.10; Supplementary Table 2), with high SiO_2 (72.50–82.54 wt%), F (0.08–0.67 wt%), and alkali contents ($Na_2O + K_2O$ = 6.36–8.78 wt%) but low contents of MgO (0.02–0.38 wt%), Fe_2O_3 (0.44–2.02 wt%), and TiO_2 (<0.18 wt%). From the biotite granite to the two-mica granite to the muscovite granite, the TiO_2, MgO, P_2O_5, CaO, and F contents decrease gradually with decreasing Fe_2O_3 contents (Fig. 3), consistent with previous data reported by Guo et al. (2012). The two greisen samples display higher contents of SiO_2 (79.81–81.42 wt%) but lower contents of Al_2O_3 (8.98–9.74 wt%), MgO (0.06–0.09 wt%), MnO (0.15–0.19 wt%), TiO_2 (0.02–0.03 wt%), CaO (0.21–1.64 wt%), and alkalis ($Na_2O + K_2O$ = 3.37–3.38 wt%) than the granite samples (Supplementary Table 2; Fig. 3). The greisen samples have high Fe_2O_3 (3.28–3.36 wt%)

and F (1.05–1.22 wt%) contents (Fig. 3), due to abundant lithian siderophyllite, wolframite, and fluorite.

The granite and greisen samples have a narrow range of REE concentrations (80.4–129 ppm; Supplementary Table 2) and similar chondrite-normalized REE patterns with strong negative Eu anomalies (Eu/Eu* = 0.01–0.31) and a weak lanthanide tetrad effect, consistent with previous data reported by Guo et al. (2012) (Fig. 4a). The $[La/Yb]_N$ and Eu/Eu* values decrease following the sequence of biotite granite, two-mica granite, muscovite granite, and greisen. The muscovite granite and greisen are depleted in LREEs and Eu, but enriched in HREEs, and this differs from the typical "wing-shaped" REE patterns for highly evolved granites (Irber 1999; Li et al. 2015). In the multi-element diagrams normalized to the mean composition of upper continental crust, all the samples are enriched in Cs (11.1–73.5 ppm), Rb (312–1020 ppm), W (4.82–65.3 ppm), Ta (3.35–27.2 ppm), Sn (5.65–198 ppm), and Li (37.8–987 ppm), but depleted in Ba (3.31–266 ppm), Sr (1.31–90.6 ppm), P (9.29–204 ppm), and Ti (12.1–1069 ppm) (Fig. 4b). Overall, the muscovite granite and greisen have much higher Li, Cs, Rb, and Sn abundances but lower Ba, Sr, and P than the biotite granite and two-mica granite.

MINERAL COMPOSITIONS

Mica

Most micas in the biotite granite and two-mica granite are homogeneous in their chemical compositions, but those in the muscovite granite and greisen show compositional zoning with distinct core and rim on BSE images or have a porous rim due to dissolution (Fig. 5). A total of 267 EPMA analyses were performed on eight samples, along with 76 LA–ICP–MS analyses on the same spots previously analyzed by EPMA. Altogether, these analyses cover all the rock types in the pluton and different areas of compositionally zoned mica grains (Supplementary Table 6).

The micas in the Xihuashan pluton show a wide range of elemental compositions. Siderophyllite in the biotite granite has the highest contents of FeO^{Tot} (21.70–24.57 wt%, 2.757–3.253 apfu), TiO_2 (0.53–3.20 wt%, 0.061–0.373 apfu), and MgO (3.96–5.12 wt%, 0.925–1.165 apfu) of all the micas, but the lowest contents of SiO_2 (34.44–37.00 wt%, 5.469–5.667 apfu) and Al_2O_3 (16.34–20.77 wt%, 2.333–2.531 apfu) (Fig. 6; Supplementary Table 6). In the two-mica granite, the lithian siderophyllite has higher contents of FeO^{Tot} (19.40–23.17 wt%, 2.439–3.002 apfu) and TiO_2 (0.03–1.57 wt%, 0.004–0.183 apfu) than the muscovite (FeO^{Tot} = 5.00–8.85 wt%, 0.576–1.051 apfu; TiO_2 = 0.01–0.40 wt%, 0.001–0.042 apfu). Micas in the muscovite granite and greisen have lower contents of FeO^{Tot} (3.43–19.97 wt%, 0.388–2.504 apfu), TiO_2 (below the detection limit to 0.51 wt%, bdl.–0.058 apfu), and MgO (0.04–0.70 wt%, 0.008–0.147 apfu), but higher contents of SiO_2 (37.77–47.99 wt%, 5.683–6.529 apfu) than those in the biotite granite and two-mica granite (Fig. 6). Micas in the biotite granite, two-mica granite, and muscovite granite have similar F contents, all of which are lower than the value of the cores of greisen micas (Fig. 6). Micas in all samples have extremely low Cl contents (mostly less than 0.06 wt%), which decrease roughly from siderophyllite, lithian siderophyllite, and muscovite along with a negative correlation with SiO_2

contents (Fig. 6f).

Micas in the biotite granite have much higher V, Sc, Cr, Co, and Ni contents than the micas in other rocks (Fig. 7a; Supplementary Table 6). Overall, the micas in the Xihuashan pluton have high contents of Rb, Cs, Nb, and Ta (typically Rb > 1000 ppm, Cs > 200 ppm, Nb > 20 ppm, Ta > 10 ppm) but the contents of most REEs are below detection limits (Supplementary Table 6). The lithian siderophyllites in the two-mica granite and the cores of micas in the muscovite granite and greisen have higher Rb and Cs contents than siderophyllites in the biotite granite (Fig. 7b, c), while the Nb and Ta contents of micas increase from the biotite granite to the two-mica granite, but decrease slightly in the greisen (Fig. 7d, e). Micas in the muscovite granite and greisen have lower Nb/Ta ratios (0.84–5.63) than siderophyllites in the biotite granite and lithian siderophyllites in the two-mica granite (Nb/Ta = 1.77–17.15) (Fig. 7f). The Sn and W contents of micas in the analyzed samples increase gradually from the biotite granite to the two-mica granite and to the cores of micas in the muscovite granite.

The micas in the muscovite granite and greisen generally exhibit core–rim zonation on BSE images (Fig. 5). The cores of zoned micas in the muscovite granite and greisen commonly have lower SiO_2 (37.77–42.47 wt%, 5.683–6.333 apfu) and Al_2O_3 (23.33–26.91 wt%, 1.667–2.317 apfu) contents but higher FeO^{Tot} (11.32–19.97 wt%, 1.356–2.504 apfu), Li_2O (0.26–1.74 wt%, 0.141–1.023 apfu), F (0.73–4.26 wt%, 0.342–1.981 apfu), Rb (4753–5860 ppm), Cs (377–1691 ppm), Ta (15.8–171 ppm), and Nb (33.9–195 ppm) contents than the rims (Figs 5, 6e, 7b–e; Supplementary Table 6). The cores of zoned micas in the muscovite granite and greisen have lower Nb/Ta ratios

(0.97–1.55 and 0.84–2.14, respectively) than the rims (1.29–5.63 and 2.01–3.40) (Fig. 7f). In addition, the mica cores in the muscovite granite have higher W (70–84 ppm) and Sn (694–848 ppm) contents than the rims (14.9–63 ppm and 265–694 ppm, respectively). The zoned micas in the greisen samples exhibit an increasing trend of W and Sn from core to rim, with values higher than the rims of zoned micas in the muscovite granite (Fig. 7g, h).

Siderite

All the siderites in the muscovite granite and greisen samples occur along the cleavages or the crystal borders of zoned micas (Fig. 5), which were most likely formed as secondary minerals due to the presence of CO_2-rich hydrothermal fluids (Buckley and Woolley 1990). The siderites were identified using Raman spectroscopy and EPMA. The Raman spectrum of the investigated mineral shows a strong intensity band at 1081.73 cm^{-1} and a low intensity band at 276.97 cm^{-1} (Fig. 8), corresponding to the symmetric stretching and external vibration of the CO_3 group, respectively, which are consistent with the characterization of carbonates reported by Buzgar and Apopei (2009). Minor shifts in position may be due to the effect of natural impurities in the studied samples. The siderites have high contents of FeO (30.14–56.01 wt%), MnO (3.47–20.39 wt%), and CO_2 (35.29–37.60 wt%), but low contents of MgO (<0.22 wt%) and alkalis ($Na_2O + K_2O < 1$ wt%) (Supplementary Table 7). The siderites in the muscovite granite have higher REE contents (ΣREE = 62–109 ppm) than those in the greisen (ΣREE = 6.92–34.4 ppm; Supplementary Table 8). They show chondrite normalized LREE-depleted and HREE-enriched pattern with very low values of $[La/Yb]_N$ (0.01–0.05) (Fig. 8c; Supplementary Table 8) and strongly negative Eu anomalies (Eu/Eu* < 0.32; Fig. 8c; Supplementary Table 8). On the multi-element diagram normalized to average upper continental crust, the siderites are enriched in Li, Rb, Cs, Ta, W, and Sn, but depleted in Ba, Zr, and Ti, similar to the whole rock composition (Fig. 8d).

DISCUSSION

Estimation of lithium contents in micas

The Li_2O content of mica may be measured directly by LA–ICP–MS or estimated by EPMA from empirical equations based on the crystallochemical relationship between Li and other major elements in the mica. Considering the different beam sizes of the LA–ICP–MS (e.g., 42 μm) and EPMA (e.g., 1 μm) methods, the Li_2O content of mica estimated from the EPMA results using empirical equations may provide a better constraint on the compositional variation at the micrometer scale.

The micas in the Xihuashan pluton display two trends on the diagram of SiO_2 versus Li_2O with contents measured by LA–ICP–MS (Fig. 9a). Siderophyllites in the biotite granite and lithian siderophyllites in the two-mica granite have relatively low SiO_2 contents that show a positive correlation with Li_2O (Fig. 9a), which is consistent with the regression function between Li_2O and SiO_2 (Fig. 9a) for trioctahedral micas (Tischendorf et al. 1997):

$$Li_2O = 0.289 \times SiO_2 - 9.658 \qquad (1)$$

In contrast, muscovites in the two-mica granite and micas in the muscovite granite and greisen have relatively higher SiO_2 contents that show a negative correlation with Li_2O contents (Fig. 9a). In particular, muscovites in the two-mica granite and the cores of micas in the muscovite granite show good correlation with the regression function between Li_2O and F (Fig. 9b) for dioctahedral micas (Tischendorf et al. 1997):

$$Li_2O = 0.3935 \times F^{1.326} \qquad (2)$$

while micas in the greisen samples clearly deviate from this function (Fig. 9b). The Li contents of hydrothermal micas (e.g., micas in the greisen) appear to be overestimated using Eq. (2) for dioctahedral micas (Fig. 9b). While the equations in Tischendorf et al. (1997) were designed for magmatic systems, additional adjustment is required for application to hydrothermal systems (Legros et al. 2016). In this paper, a new empirical equation for the Li_2O and F contents of hydrothermal micas is introduced (Fig. 9c):

$$Li_2O = 0.0748 \times F^2 + 0.0893 \times F \qquad (3)$$

This equation may be used for estimating the Li_2O content of hydrothermal mica from the F content determined by EPMA. The Li contents calculated with this equation are in agreement with the values measured by LA–ICP–MS ($R^2 = 0.82$) (Fig. 9d).

The Li_2O contents determined using EPMA indicate that the biotites in the biotite granite and two-mica granite are siderophyllite and protolithionite (lithian siderophyllite), respectively, which is consistent with the trend of magmatic evolution (Fig. 10). Lithian siderophyllites in the greisen have higher Li_2O contents (1.57–1.74 wt%) than those in the two-mica granite (0.88–1.33 wt%). They are protolithionites following the classification proposed by Tischendorf et al. (1997) (Fig. 10a).

Alternatively, they belong to the transitional series between dioctahedral and trioctahedral micas based on Foster (1960) (Fig. 10b), also termed the ferrous aluminum micas in Monier and Robert (1986). Muscovites in the two-mica granite, muscovite granite, and greisen all belong to the transitional series, but in their octahedral sites they have lower contents of Li_2O and divalent metal cations (Fe^{2+}, Mn^{2+}, Mg^{2+}) than the lithian siderophyllites in the greisen (Fig. 10b).

Variation of halogens in the melts and fluids

The micas display a wide range of F contents (0.41–4.26 wt%). Overall, the siderophyllites in the biotite granite have the lowest F contents (0.84–1.95 wt%), while micas in the greisen have the highest (up to 4.26 wt%). The cores of zoned micas in the muscovite granite and greisen typically have higher F contents (0.73–4.26 wt%) than the rims (0.41–3.46 wt%) (Supplementary Table 6). In addition, the micas have much lower Cl contents (up to 0.06 wt%) than F (0.41–4.26 wt%; Supplementary Table 6). Indeed, the substitution of Cl into the OH site of mica is much less favorable than the substitution of F (Munoz 1992), due to the significantly larger ionic radius of Cl^- (1.81 Å; cf. F^- = 1.31 Å and OH = 1.38 Å).

The exchange of F, Cl, and OH between micas and associated fluids may be used to obtain the halogen fugacity of the fluids (Munoz 1984) as well as the halogen concentrations in the melt (Zhang et al. 2012). Since the measured Cl contents of the Xihuashan micas are extremely low (mostly less than 0.06 wt%, with large errors of 10%–15%), the exchange of Cl and OH between micas and associated fluids is not further discussed.

The equations used for estimating the F fugacity of a fluid [log(fH_2O/fHF)] and the F concentration in a melt (W_F^m) are listed as follows (Munoz 1984; Zhang et al. 2012):

$$\log\left(\frac{fH_2O}{fHF}\right) = \frac{1000}{T} \times \left(2.37 + 1.1X_{Mg}\right) + 0.43 - \log\left(\frac{X_F}{X_{OH}}\right)^{mica} \qquad (4)$$

$$W_F^m = \frac{1}{1+\frac{fH_2O}{fHF}} \times \frac{19}{18.02} \times \frac{10^6}{0.000943 \times T - 0.574} \qquad (5)$$

where X_F and X_{OH} are the mole fractions of F and OH in the hydroxyl site of mica, respectively, X_{Mg} is the mole fraction of Mg in the octahedral site of mica, and T is the crystallization temperature of mica in degrees Kelvin. Due to the difficulties in calculating the crystallization temperatures of micas directly, the homogenization temperatures of fluid inclusions (Mu et al. 1982; Zhang et al. 1982; Wei et al. 2011) and melt inclusions (Chang and Huang 2002) in the Xihuashan tungsten deposit were adopted to estimate the F fugacity of the fluids and the F content of the melt. The melt inclusions in beryl from the wolframite–quartz veins in the Xihuashan tungsten deposit gave a homogenization temperature of 720 °C (Huang et al. 2006), consistent with the mean value (703 ± 28 °C; range of 643 to 890 °C) of the temperature given by the Ti-in-zircon thermometer for the Xihuashan granites (Yang et al. 2018), which can be regarded as the crystallization temperature of the Xihuashan granitic magma. In addition, there were two generations of fluid in the Xihuashan granites, based on stable oxygen isotope data from fluid inclusions (Mu et al. 1982; Zhang et al. 1982; Wei et al. 2011). The primary ore-fluid had a temperature of 370 ± 30 °C (fluid of magmatic origin, $\delta^{18}O$

= 10‰–13‰) and the late fluid had a temperature of 220 ± 10 °C (meteoric water, $\delta^{18}O$ = –8.7‰ to +3.1‰). It is assumed that the primary ore-fluid was related to the formation of the cores of zoned micas in the greisen and that the late fluid was related to the rims of zoned micas in the muscovite granite and greisen, and this will be discussed later. The results of calculations using Eq (4) and Eq (5) are given in Supplementary Table 6 and shown on Fig. 11. Overall, the log(fH_2O/fHF) values of the fluid decrease from the greisen (4.15–4.65, mean = 4.33) to the biotite granite (3.95–4.42, mean = 4.14) to the two-mica granite (3.38–3.82, mean = 3.65), and to the muscovite granite (3.26–3.91, mean = 3.56) (Fig. 11a). In general, F is preferentially concentrated in a residual melt when the volatiles of a hydrous magma are exsolved (Zhu and Sverjensky 1992). The loss of volatiles from a hydrous magma will enhance the F content in the residual melt, producing a lower OH/F value in the melt but a higher OH/F ratio in the associated fluid. This implies that the F content (W_F^m values) of the melt increases gradually from the biotite granite to the two-mica granite, and to the muscovite granite (Fig. 11c).

With regard to the zoned micas in the muscovite granite and greisen, the fluids related to the rims always have higher log(fH_2O/fHF) values than those related to the cores (Fig. 11a). In addition, the rims of micas in the muscovite granite and greisen all have higher Fe^{3+}/Fe^{2+} ratios than the cores (Fig. 11b). As the Fe^{3+}/Fe^{2+} ratio shows a positive correlation with temperature (Wones and Eugster 1965), the higher Fe^{3+}/Fe^{2+} ratios of the rims of zoned micas cannot be attributed to lower temperatures relative to the magmatic cores, but an increasing oxygen fugacity and H_2O content.

Magmatic evolution of the Xihuashan intrusive rocks

The Xihuashan granites have extremely variable whole-rock and mineral compositions, indicating that the rocks might have undergone varying degrees of fractional crystallization.

The micas show a wide range of compositions (Fig. 10) from siderophyllite to lithian siderophyllite, which corresponds to the evolution of the magma from the biotite granite to the two-mica granite. As a peraluminous melt system evolves, Rb and Cs are compatible in biotite while Y, Th, and REEs are incompatible (Bea et al. 1994). The micas in our samples have low Y, Th, and REE contents but extremely high Rb and Cs contents (Supplementary Table 6), suggesting that fractionation of the micas was insignificant during the magmatic evolution. The increase of Rb and Cs contents with decreasing K/Rb ratios from the biotite granite to the two-mica granite (Fig. 12a, b) further excludes the possibility of significant mica fractionation during the magmatic evolution of the Xihuashan intrusive rocks. With regard to the feldspars, Rb and Cs are compatible in K-feldspar but incompatible in plagioclase (Bea et al. 1994), and an increase of Rb and Cs in micas from the biotite granite to the two-mica granite (Fig. 7b, c) could be attributed to a remarkable fractionation of plagioclase. It is also consistent with the fact that our samples are notably enriched in Li, Rb, and Cs compared with upper continental crust (UCC) (Fig. 4b). In addition, xenotime rather than apatite is the principal phosphate mineral in Ca-poor peraluminous granitic melts (Wang et al. 2003). In the Xihuashan pluton, the two-mica granite and muscovite granite samples contain abundant xenotime with apatite being absent or rare, which indicates an essentially Ca-poor peraluminous melt. The Ca-poor melt would have been the product of the fractional crystallization of Ca-rich minerals, including apatite and plagioclase. However, apatite fractionation, if it existed, could not have been primarily responsible for producing the Ca-poor peraluminous melt, because it would have required a large amount of phosphorus to exhaust the Ca in the system. Therefore, the presence of abundant xenotime in the two-mica granite and muscovite granite may provide evidence for plagioclase fractionation during the magmatic evolution, which is consistent with decreasing MgO, TiO_2, Fe_2O_3 and CaO (Fig. 3) and gradually pronounced Eu negative anomalies (Fig. 4a) from biotite granite to two-mica granite to muscovite granite.

Collectively, the variations in composition of mica in the Xihuashan pluton are consistent with a trend of magmatic evolution from the biotite granite to the two-mica granite to the muscovite granite. This evolutionary process was controlled mainly by the fractional crystallization of plagioclase.

The hydrothermal evolution recorded in zoned micas and siderite

Micas in highly evolved granites and pegmatites always show compositional zoning as a result of the evolution of the magma or sub-solidus fluid interactions (Roda–Robles et al. 2007; Van Lichtervelde et al. 2008; Li et al. 2015). Volatile components (e.g., H_2O, F, B, and P) and lithophile rare metal elements (e.g., Li, Rb, Cs, Ta, Nb, Sn, and W) are incompatible in major rock-forming minerals during the evolution of peraluminous melt systems. Accordingly, the Li_2O, F, Rb, Cs, Nb, and Ta contents of mica may increase with the progressive evolution of the magma (Roda–Robles et al. 2007), leading to differences in brightness in the zoning textures revealed by the BSE images (Fig. 5). Since fluorine is concentrated in the melt during the differentiation of a granitic melt when there is lack of fractionation of fluorine-enriched minerals such as apatite and mica (Li et al. 2015), the supercritical fluids exsolved from a highly fractionated Sn–W granitic magma are usually enriched in F (Thomas et al. 2005). The addition of F into the melt may increase the abundance of non-bridging oxygens (NBOs), which increases the proportion of WO_4^{2-} tetrahedra in silicate melt. Indeed, with our samples, the log(fH_2O/fHF) values decrease and the W_F^m values increase from the biotite granite to the two-mica granite and the muscovite granite (Fig. 11), consistent with an evolution of magma without involvement of any notable fractionation of apatite or mica. However, the rims of the zoned micas in the muscovite granite and greisen have lower Li_2O, Rb, Cs, Nb, Ta, and F contents but higher Si and Al contents than the cores (Fig. 9; Supplementary Table 6). Moreover, the rims of the zoned micas belong to the transition series (Fig. 10), similar to the ferrous aluminum micas described by Monier and Robert (1986), which were the products of metasomatic alteration. Altogether, the characteristics of the compositional zoning and dissolution textures (Fig. 5) of the micas in our samples indicate that they were produced by fluid–rock interactions rather than melt differentiation. Furthermore, the micas would have been enriched in F when they interacted with supercritical fluids exsolved from a highly differentiated magma. The rims of the zoned micas show significant depletion in F (Supplementary Table 6), corresponding to higher log(fH_2O/fHF) values than the mica cores, and this suggests a process of subsolidus replacement by a dominantly external aqueous fluid.

The siderites have variable REE contents (ΣREE = 6–110 ppm; Supplementary Table 8) and negative Eu anomalies, which would have been caused by the fluids having variable REE contents or pH values (Michard 1989; Möller et al. 2004). In general, the total REE content of hydrothermal solutions increases with decreasing pH values (Michard 1989; Möller et al. 2004). In acidic solutions, LREEs are likely to be enriched in aqueous phases, while HREEs are preferentially adsorbed on mineral surfaces (Schwinn and Markl 2005). Thus, siderites precipitated from fluids with variable pH values would have variable LREE/HREE ratios. The siderites in our samples of muscovite granite and greisen have similar $(La/Yb)_N$ ratios. Instead, different sources of fluid with variable REE contents are more likely to have been responsible for the wide range of REE contents that characterizes the siderites, and this is consistent with the $\log(fH_2O/fHF)$ values of the rims of zoned micas in the greisen being generally lower than those in the muscovite granite (Fig. 11).

The stability of siderite depends on the CO_2 fugacity and the oxygen fugacity (Fusswinkel et al. 2013). Siderite is stable under conditions of low oxygen fugacity (i.e., fO_2 = –38 to –54) and high CO_2 fugacity (i.e., fCO_2 = –1 to +2) (Fusswinkel et al. 2013). It is replaced by magnetite in the reaction "6 Siderite + O_2 = 2 Magnetite + 6 CO_2" when the oxygen fugacity increases or the activity of CO_2 decreases (Hovis et al. 1991). The lack of magnetite in the muscovite granite and greisen (Table 1) may be attributed to a relatively reducing environment where the siderite crystals were stable. Therefore, the presence of siderite in the Xihuashan granite indicates a reducing environment during the fluid–rock interactions, and the oxygen fugacity (fO_2) would have been close to the value constrained by the "C + O_2 = CO_2" buffer (Yang et al. 2013).

The fluids associated with the tungsten mineralization would have been of external origin or exsolved from the melt (e.g., Wang et al. 2003; Wei et al. 2012; Harlaux et al. 2018). It is noteworthy that the cores of zoned micas in the greisen and muscovite granite show much lower log(fH_2O/fHF) values and Fe^{3+}/Fe^{2+} ratios than the rims (Fig. 11), and this indicates that the fluids associated with the formation of the greisen and muscovite granite had a higher fluorine fugacity and were even more reducing than the fluids associated with the fluid–rock interactions. Such fluids might have been supercritical fluids exsolved from the highly fractionated magma, and this is consistent with the observation that the log(fH_2O/fHF) values associated with the cores of micas in the greisen are close to those associated with magmatic micas in the granite samples (Fig. 11a, b). In addition, based on the fluid inclusion studies, Wei et al. (2012) proposed that a mixture of fluids from two different sources could have been responsible for the deposition of wolframite in the Xihuashan deposit. Fluids with a low oxygen fugacity and enriched in fluorine may be derived from fluid oversaturation of a granitic melt (Maruejol et al. 1990; Wang et al. 2003), which may contribute to the formation of the cores of zoned micas in the greisen and muscovite granite. The fluid-rock interactions, however, involved mainly meteoric fluids that were associated with alteration of early Li-rich micas into late muscovite (Legros et al. 2016). These fluids were also enriched in H_2O and CO_2, as recorded in the rims of zoned mica and the siderite in the greisen and muscovite granite. In particular, the rims of zoned micas in the greisen samples have lower log(fH$_2$O/fHF) values than those in the muscovite granite samples, which further indicates that the fluids associated with the greisen contained larger amounts of magma-derived fluids.

Tungsten enrichment during the evolution of the magmatic–hydrothermal system

Tungsten deposits are usually associated with fractionated granitic magmas and hydrothermal processes (e.g., Xie et al. 2016; Breiter et al. 2017). In peraluminous granitic systems, tungsten commonly behaves as an incompatible element for most rock-forming minerals and accumulates in melts during fractional crystallization (Hulsbosch et al. 2016). The WO$_3$ content of columbite-group minerals increases from 5 to 15 wt% during magma evolution (Xie et al. 2018), which confirms that tungsten can be concentrated in melts. In addition, mica may be used as an indicator of ore-forming potential for tungsten granites (Yin et al. 2019). In the Xihuashan granite, the tungsten content of micas increases from the biotite granite (0.36–12.8 ppm) to the muscovite granite (14.9–84.1 ppm) while the K/Rb ratio of micas decreases (Fig. 12c), consistent with the trend of magma evolution. However, magmatic wolframite can crystallize directly from a highly evolved granite melt under restricted conditions, as for example from a peraluminous melt with high concentrations (6 wt%) of fluxing compounds (B, Li, F, and P) and with crystallization temperatures lower than 550 °C at 800 bars (Che et al. 2013). In most cases, the required conditions for saturation of magmatic wolframite cannot be reached in granitic melts due to the low levels of fluxing compounds. It is rare to have a wolframite of purely magmatic origin, and hydrothermal fluids typically play a significant role in W mineralization. In the Xihuashan granite, the lack of wolframite in the muscovite granite suggests that the tungsten concentration in the melts did not become saturated relative to wolframite as a result of magmatic fractionation. Indeed, the whole-rock content of W in the Xihuashan granite (4.82–65.3 ppm) is much lower than the solubility of wolframite in peraluminous granitic melts (~1000 ppm WO_3 at 750–800 °C; Štemprok 1990). Therefore, although tungsten may be concentrated in a melt via magmatic fractionation, in the magmas of the Xihuashan pluton the W contents were always much lower than the oversaturation level during the evolution of the magma.

Hydrothermal activities may play an important role in W mineralization (e.g., Štemprok 1990; Li et al. 2018). The wolframite crystals in the greisen are intergrown with zoned mica (Fig. 5d), and they would have formed during hydrothermal activity. However, wolframite is absent from the muscovite granite, even though the abundant zoned micas with dissolution textures (Fig 5a, b) provide evidence of fluid alteration. The rims of zoned micas in the muscovite granite have lower W contents than the cores (Fig. 7f), which was probably due to hydrothermal alteration. The hydrothermal fluids liberated W from the micas and resulted in formation of a W-depleted rim, whereas W was concentrated in the hydrothermal fluid. The elevated CO_2 concentration may increase the acidity of fluid and the solubility of tungstates, which facilitates concentrating W in the fluids (Liu et al. 2017; Wang et al. 2020). The rims of zoned micas in the greisen have higher W contents than those in the muscovite granite (Fig.

7f), which was probably due to different CO_2 and W concentrations in the hydrothermal fluids. The W-rich rims of zoned mica in the greisen clearly show the involvement of W-rich fluids in the formation of the tungsten deposit (Figs 5d, 7h). Furthermore, a fluid rich in F, Li, and rare metals can induce greisenization in the upper part of the granitic cupola, causing dissolution of feldspars and crystallization of new quartz, zinnwaldite, fluorite, and topaz (Breiter et al. 2017). Greisenization consumes H^+ and increases the pH value of fluids following the reaction:

$$2Na[AlSi_3O_8] + K[AlSi_3O_8] + 2H^+ = KAl_2[AlSi_3O_{10}](OH)_2 + 6SiO_2 + 2Na^+$$

Albite K-feldspar Muscovite Quartz

An increase in fluid pH during greisenization will destabilize the polymeric tungstates to form WO_4^{2-} and other monomeric tungstates (Wang et al. 2020), which may interact with metal cations (i.e., Fe, Mn or Ca) to form wolframite or scheelite. Thus, greisenization promoted the generation of WO_4^{2-} in the fluids, and potentially contributed to the formation of tungsten deposit (Audétat et al. 2008; Harlaux et al. 2017; Legros et al. 2019).

IMPLICATIONS FOR TUNGSTEN MINERALIZATION

The hydrothermal fluid related to the W deposits would have different sources, including an early magmatic fluid and a later metamorphic or meteoric fluid (Wei et al. 2012; Hulsbosch et al. 2016). However, the signature of the early magmatic fluid is usually overprinted by the metamorphic or meteoric fluid (Wei et al. 2012; Hulsbosch et al. 2016). Thus, attempts to determine whether a magmatic or metamorphic fluid was responsible for W mineralization associated with a granite typically provide inconclusive results. In the Xihuashan tungsten granite, the composition and zoning texture of micas may provide some valid constraints on the nature of fluids and the mechanism for precipitation of wolframite. The interaction between external aqueous fluids and pre-existing micas has played an important role in leaching the ore-forming elements (i.e., W and Fe) from the micas into the fluids, which is proved by remarkably dropped concentrations of W and Fe from the cores to the rims of zoned micas in the muscovite granite (Figs 6c, 7h). The W-rich rims of the zoned mica in the greisen, together with the high whole-rock F contents (up to 1.22 wt%) of greisen samples, demonstrate that the fluid related to the greisenization was enriched in F and W. The F-rich fluids involved in the greisenization were most likely derived from the oversaturation of a rare-metal granitic melt (Maruéjol et al. 1990; Launay et al. 2018; Legros et al. 2018). Therefore, the rims of zoned mica in the greisen are enriched in W due to the effect of W-rich fluids, whereas the rims of zoned mica in the muscovite granite are related to the dominant external fluids that had much lower W contents. This difference between the zoned micas in the greisen and muscovite granite indicates that the process of greisenization was critical for extracting and transporting the W from the melts/rocks into the fluids (Launay et al. 2018).

The processes identified in the Xihuashan tungsten granite may have been active in many wolframite-bearing quartz-vein deposits elsewhere. Some famous metallogenic provinces or plutons, such as the French Massif Central, the Erzgebirge, the northern Canadian Cordillera, Iberian Massif and the Nanling and Dahutang mineralization regions in South China, are closely related to magmatic and hydrothermal processes (e.g., Legros et al. 2016, 2018; Breiter et al. 2017a, b; Legro et al. 2016, 2018; Xie et al. 2018; Yin et al. 2019). Furthermore, the micas in these tungsten-bearing granites are commonly zoned and enriched in fluxing compounds (e.g., Breiter et al. 2017; Harlaux et al. 2018a; Xie et al. 2018; Yin et al. 2019), which might also record the processes of tungsten mineralization related to fluids during their evolution through the magmatic–hydrothermal transition. Collectively, the external and magmatic fluids all facilitated the tungsten mineralization. The overall scenario of the ore-forming processes for the Xihuashan tungsten deposit is summarized as follows (Fig. 13):

1) The W and F were gradually concentrated in the magmatic fluids via magmatic fractionation.

2) The W and F-rich magmatic fluids pooled in the granitic cupola and induced greisenization. This process destabilized the polymeric tungstates to form WO_4^{2-} in the fluids.

3) The pooled fluid flow might have been overpressured, eventually being injected into the vein system.

4) Tungsten and the fluids would have migrated along faults and fractures with tungsten being precipitated as vein-type wolframite at favorable sites when the W and F-rich fluid was mixed with an external meteoric fluid.

Therefore, tungsten mineralization is closely related to the mixture of magmatic and external fluids. Furthermore, the presence of siderite in the greisen and muscovite granite indicates that the fluids are rich in Fe and Mn, which are ore-forming elements generating metal complexes with WO_4^{2-} during the precipitation of wolframite.

The input of Fe and Mn in the fluids would be attributed to the reactions between external CO_2-bearing fluid and host-rock (Lecumberri-Sanchez et al., 2017; Wang et al. 2020). In addition, the fluid boiling process might also take the role of triggering the precipitation of wolframite, as the transport of volatile elements (e.g., CO_2, H^+) into vapor phase changes the chemical composition of the fluid (Korges et al., 2018).

ACKNOWLEDGEMENTS

We thank C.Y. Li, Y. Liu and X.L. Tu for analytical assistance. We are also grateful to Dr. M. Harlaux and an anonymous reviewer for their careful reviews and constructive comments, which strongly improved the manuscript. This study was financially supported by the National Key Research and Development Program of China (No. 2016YFC0600204) and National Natural Science Foundation of China (NSFC Projects 41625007, U1701641). This is contribution No. IS-xxxx from GIG-CAS.

REFERENCES CITED

Akoh, J.U., and Ogunleye, P.O. (2014) Mineralogical and geochemical evolution of muscovite in the pegmatite group of the Angwan Doka area, Kokoona district: A clue to petrogenesis and tourmaline mineralization potential. Journal of geochemical exploration, 146, 89–104.

Audétat, A., Pettke, T., Heinrich, C.A., and Bodnar, R.J. (2008) The composition of magmatic-hydrothermal fluids in barren and mineralized intrusions. Economic Geology, 103, 877–908.

Bau, M., and Möller, P. (1992) Rare earth element fractionation in metamorphogenic hydrothermal calcite, magnesite and siderite. Mineralogy and Petrology, 45(45), 231–246.

Bau, M. (1996) Controls on the fractionation of isovalent trace elements in magmatic and aqueous systems: Evidence from Y/Ho, Zr/Hf, and lanthanide tetrad effect. Contributions to Mineralogy and Petrology, 123, 323-333.

Bea, F., Pereira, M.D., and Stroh, A. (1994) Mineral/leucosome trace-element partitioning in a peraluminous migmatite (a laser ablation-ICP-MS study). Chemical Geology, 117(1–4), 291–312.

Breiter, K., Ďurišová, J., Hrstka, T., Korbelová, Z., Vaňková, M.H., Galiová, M.V., Kanicky, V., Rambousek, P., Knésl, I., Dobeš, P., and Dosbaba, M. (2017) Assessment of magmatic vs. metasomatic processes in rare-metal granites: A case study of the Cínovec/Zinnwald Sn-W-Li deposit, Central Europe. Lithos, 292–293, 198–217.

Buzgar, N., and Apopei, A.I. (2009) The Raman study of certain carbonates. Geologie. Tomul LV, 2, 97–112.

Buckley, H.A., and Woolley, A.R. (1990) Carbonates of the magnesite-siderite series from four carbonatite complexes. Mineralogical Magazine, 54(376), 413–418.

Castorina, F., and Masi, U. (2008) REE and Nd-isotope evidence for the origin of siderite from Jebel Awan deposit (Central Morocco). Ore Geology Reviews, 34, 337-342.

Chang, H.L., and Huang, H.L. (2002) A preliminary investigation of melt inclusions and genesis of Xihuashan tungsten deposit. Acta Petrologica et Mineralogica, 21(2), 143-150 (in Chinese with English abstract).

Che, X.D., Linnen, R.L., Wang, R.C., Aseri, A., and Thibault, Y. (2013) Tungsten solubility in evolved granitic melts: An evaluation of magmatic wolframite. Geochimica et Cosmochimica Acta, 106: 84–98.

Deng, X.D., Luo, T., Li, J.W. and Hu, Z.C., (2019) Direct dating of hydrothermal tungsten mineralization using in situ wolframite U–Pb chronology by laser ablation ICP-MS. Chemical Geology, 515, 94–104.

El Korh, A., Boiron, M.C., Cathelineau, M., Deloule, E., and Luais, B. (2020) Tracing metallic pre-concentrations in the Limousin ophiolite-derived rocks and Variscan granites (French Massif Central). Lithos, 356, 105345.

Foster, M.D. (1960) Interpretation of the composition of trioctahedral micas. US Geological Survey Professional Paper, 354-E, 115–147.

Fusswinkel, T., Wagner, T., Wenzel, T., Wälle, M., and Lorenz, J. (2013) Evolution of unconformity-related MnFeAs vein mineralization, Sailauf (Germany): Insight from major and trace elements in oxide and carbonate minerals. Ore Geology Reviews, 50, 28–51.

Gleeson, S.A., Wilkinson, J.J., Stuart, F.M., and Banks, D.A. (2001) The origin and evolution of base metal mineralizing brines and hydrothermal fluids, South Cornwall, UK. Geochimica et Cosmochimica Acta, 65, 2067–2079.

Guo, C.L., Chen, Y.C., Zeng, Z.L., and Lou, F.S. (2012) Petrogenesis of the Xihuashan granites in southeastern China: Constraints from geochemistry and in-situ analyses of zircon U-Pb-Hf-O isotopes. Lithos, 148, 209–227.

Harlaux, M., Mercadier, J., Marignac, C., Peiffert, C., Gloquet, C., and Cuney, M. (2018a) Tracing metal sources in peribatholitic hydrothermal W deposits based on the chemical composition of wolframite: The example of the Variscan French Massif Central. Chemical Geology, 479, 58–85.

Harlaux, M., Romer, R.L., Mercadier, J., Morlot, C., Marignac, C., and Cuney, M. (2018b) 40 Ma of hydrothermal W mineralization during the Variscan orogenic evolution of the French Massif Central revealed by U-Pb dating of wolframite. Mineralium Deposita, 53(1), 21–51.

Harlaux, M., Mercadier, J., Bonzi, W.M.E., Kremer, V., Marignac, C. and Cuney, M. (2017) Geochemical signature of magmatic-hydrothermal fluids exsolved from the Beauvoir rare-metal granite (Massif Central, France): insights from LA-ICPMS analysis of primary fluid inclusions. Geofluids, 1925817, 1-25.

Higgins, N.C. (1980) Fluid inclusion evidence for the transport of tungsten by carbonate complexes in hydrothermal solutions. Canadian Journal of Earth Sciences, 17, 823–830.

Hovis, G.L., Delbove, F., and Bose, M.R. (1991) Gibbs energies and entropies of K–Na mixing for alkali feldspars from phase equilibrium data: implications for feldspar solvi and short-range order. American Mineralogist, 76, 913–927.

Hu, R.Z., Bi, X.W., Jiang, G.H., Chen, H.W., Peng, J.T., Qi, Y.Q., Wu, L.Y., and Wei, W.F. (2012) Mantle-derived noble gases in ore-forming fluids of the granite-related Yaogangxian tungsten deposit, Southeastern China. Mineralium Deposita, 47, 623–

632.

Huang, H.L., Chang, H.L., Fu, J.M., Wang, X.W., and Li, T.Y. (2006) Formation pressure of wolframite-vein deposits and emplacement depth of related granite in Xihuashan, Jiangxi Province. Mineral Deposits, 25(5), 562–571 (in Chinese with English abstract).

Huang, H.L., Chang, H.L., Li, F., Tan, J., Zhang, C.H., Zhou, Y., Yang, K., and Yan, F. (2013) Microthermometry and characteristic element determination for the fluid inclusions in the wolframite and quartz in the drusy cavities of Xihuashan tungsten deposit. Earth Science Frontiers, 20(2), 205–212 (in Chinese with English abstract).

Hulsbosch, N., Boiron, M., Dewaele, S., and Muchez, P. (2016) Fluid fractionation of tungsten during granite–pegmatite differentiation and the metal source of peribatholitic W quartz veins: Evidence from the Karagwe-Ankole Belt (Rwanda). Geochimica et Cosmochimica Acta, 175, 299–318.

Irber, W. (1999) The lanthanide tetrad effect and its correlation with K/Rb, Eu/Eu*, Sr/Eu, Y/Ho, and Zr/Hf of evolving peraluminous granite suites. Geochimica et Cosmochimica Acta, 63(3–4), 489–508.

Jochum, K.P., Weis, U., Stoll, B., Kuzmin, D., Yang, Q., Raczek, I., Jacob, D.E., Stracke, A., Birbaum, K., Frick, D.A., and Günther, D. (2011) Determination of reference values for NIST SRM 610–617 glasses following ISO guidelines. Geostandards and Geoanalytical Research, 35(4), 397–429.

Keppler, H., and Wyllie, P.J. (1991) Partitioning of Cu, Sn, Mo, W, U, and Th between melt and aqueous fluid in the systems haplogranite-H_2O–HCl and haplogranite-H_2O-HF. Contribution to Mineralogy and Petrology, 109, 139–150.

Korges M, Weis P, Lüders V, Laurent O. (2018) Depressurization and boiling of a single magmatic fluid as a mechanism for tin-tungsten deposit formation. Geology 46: 75-78.

Launay, G., Sizaret, S., Guillou-Frottier, L., Gloaguen, E., and Pinto, F. (2018) Deciphering fluid flow at the magmatic-hydrothermal transition: A case study from the world-class Panasqueira W–Sn–(Cu) ore deposit (Portugal). Earth and Planetary Science Letters, 499, 1–12.

Le Bel, L., Li, Y.D., and Sheng, J.F. (1984) Granitic evolution of the Xihuashan-Dangping (Jiangxi, China) tuntgsten-bearing system. Tschermaks Mineralogische und Petrographische Mitteilungen, 33, 149–167.

Lecumberri-Sanchez P, Vieira R, Heinrich CA, Pinto F, Wälle M. (2017) Fluid-rock interaction is decisive for the formation of tungsten deposits. Geology 45: 579-582.

Legros, H., Marignac, C., Mercadier, J., Cuney, M., Richard, A., Wang, R.C., Charles, N., and Lespinasse, M. (2016) Detailed paragenesis and Li-mica compositions as recorders of the magmatic-hydrothermal evolution of the Maoping W-Sn deposit (Jiangxi, China). Lithos, 264, 108–124.

Legros, H., Marignac, C., Tabary, T., Mercadier, J., Richard, A., Cuney, M., Wang, R.C., Charles, N., and Lespinasse, M. (2018) The ore-forming magmatic-hydrothermal system of the Piaotang W-Sn deposit (Jiangxi, China) as seen from Li-mica geochemistry. American Mineralogist, 103(1), 39–54.

Legros, H., Richard, A., Tarantola, A., Kouzmanov, K., Mercadier, J., Vennemann, T., Marignac, C., Cuney, M., Wang, R.C., Charles, N., and Bailly, L. (2019) Multiple fluids involved in granite-related W-Sn deposits from the world-class Jiangxi province (China). Chemical Geology, 508, 92–115.

Legros, H., Harlaux, M., Mercadier, J., Romer, R.L., Poujol, M., Camacho, A., Marignac, C., Cuney, M., Wang, R.C., Charles, N., and Lespinasse, M.Y. (2020) The world-class Nanling metallogenic belt (Jiangxi, China): W and Sn deposition at 160 Ma followed by 30 my of hydrothermal metal redistribution. Ore Geology Reviews, 117, 103302.

Longerich, H.P., Jackson, S.E., and Günther, D. (1996) Laser ablation inductively coupled plasma mass spectrometric transient signal data acquisition and analyte concentration calculation. Journal of Analytical Atomic Spectrometry, 11, 899–904.

Li, J., Huang, X.L,, He, P.L., Li, W.X., Yu, Y., and Chen, L.L. (2015) In situ analyses of micas in the Yashan granite, South China: constraints on magmatic and hydrothermal evolutions of W and Ta-Nb bearing granites. Ore Geology Reviews, 65, 793–810.

Li, J., Huang, X.L., Wei, G.J., Liu, Y., Ma, J.L., Han, L., and He, P.L. (2018) Lithium isotopic fractionation during magma differentiation and hydrothermal processes in the rare-metal granites. Geochimica et Cosmochimica Acta, 240, 64–79.

Li, Q.L., Li, X.H., Lan, Z.W., Guo, C.L., Yang, Y.N., Liu, Y., and Tang, G.Q. (2013) Monazite and xenotime U–Th–Pb geochronology by ion microprobe: dating highly fractionated granites at Xihuashan tungsten mine, SE China. Contributions to

Mineralogy and Petrology, 166, 65–80.

Liu, X.C, Xing, H.L., and Zhang, D.H. (2017) Influences of hydraulic fracturing on fluid flow and mineralization at the vein-type tungsten deposits in southern China. Geofluids, 4673421, 1-11.

Li, X.H., Li, W.X., Li, Z.X., Lo, C.H., Wang, J., Ye, M.F., and Yang, Y.H. (2009) Amalgamation between the Yangtze and Cathaysia Blocks in South China: constraints from SHRIMP U–Pb zircon ages, geochemistry and Nd–Hf isotopes of the Shuangxiwu volcanic rocks. Precambrian Research, 174, 117–128.

Li, Z.X., Li, X.H., Wartho, J.A., Clark, C., Li, W.X., Zhang, C.L., and Bao, C. (2010) Magmatic and metamorphic events during the early Paleozoic Wuyi-Yunkai orogeny, southeastern South China: New age constraints and pressure-temperature conditions. Geological Society of America Bulletin, 122(5–6), 772–793.

Lin, W.W., and Peng, L.J. (1994) The estimation of Fe^{3+} and Fe^{2+} contents in amphibole and biotite from EPMA data. Journal of Changchun University of Science and Technology, 24(2), 155–162 (in Chinese with English abstract).

Linnen, R.L., and Williams-Jones, A.E. (1995) Genesis of a magmatic metamorphic hydrothermal system; the Sn-W polymetallic deposits at Pilok, Thailand. Economic Geology, 90, 1921–1935.

Linnen, R.L. and Cuney, M. (2005) Granite-related rare-element deposits and experimental constraints on Ta–Nb–W–Sn–Zr–Hf mineralization. In Rare-Element Geochemistry and Mineral Deposits. GAC Short Course Notes, vol. 17 (eds. R. L. Linnen and I. M. Samson). Geological Association of Canada, pp, 45–67.

Liu, J.Y. (2005) Composition of Xihuashan granites and its relationship to tungsten metallogenesis. Contributions to Geology and Mineral Resources Research, 20, 1–7 (in Chinese with English abstract).

Liu, Y.S., Hu, Z.C., Gao, S., Gunther, D., Xu, J., Gao, C.G., and Chen, H.H. (2008) In situ analysis of major and trace elements of anhydrous minerals by LA-ICP-MS without applying an internal standard. Chemical Geology, 257, 34–43.

Ma, W.W., Huang, X.L., Yu, Y., Yin, R., and He, P.L. (2020) Characteristics of micas in the Limu granite, South China: illuminating the hydrothermal processes related to tin mineralization. Geotectonica et Metallogenia, (accepted, in Chinese with English abstract).

Maruéjol, P., Cuney, M., and Turpin, L. (1990) Magmatic and hydrothermal R.E.E. fractionation in the Xihuashan granites (SE China). Contributions to Mineralogy and Petrology, 104, 668–680

Michard, A. (1989) Rare earth elements systematics in hydrothermal fluids. Geochimica et Cosmochimica Acta, 53, 745–750.

Möller, P., Dulski, P., Savascin, Y., and Conrad, M. (2004) Rare earth elements, yttrium and Pb isotope ratios in thermal spring and well waters of West Anatolia, Turkey: a hydrothermal study of their origin. Chemical Geology, 206, 97–118.

Monier, G., and Robert, J.L. (1986) Muscovite solid solutions in the system K_2O-MgO-FeO-Al_2O_3-SiO_2-H_2O: an experimental study at 2 kbar P_{H2O} and comparison with natural Li-free white micas. Mineralogical Magazine, 50, 257–266.

Mu, Z., Huang, F., Chen, C., Zheng, S., Fen, S., Lu, D., and Mei, Y. (1982) Oxygen, hydrogen and carbon isotope studies of Piaotang and Xihuashan quartz vein-type tungsten deposits, Jiangxi Province. In: Hepworth JV, Yu HZ (eds) Symposium on Tungsten geology, Jiangxi, China. ESCAP-RMRDC, Bandung, pp, 553–566.

Munoz, J.L. (1984) F-OH and Cl-OH exchange in micas with application to hydrothermal ore deposits. Reviews in Mineralogy, 13, 469–493.

Nie, R.F., and Wang, X.D. (2007) On research advancement of Gannan tungsten deposit. China tungsten industry 22(3), 1–5 (in Chinese with English abstract).

Pei, F.R., and Hong, D.W. (1995) New advances in the study of collision orogeny of granites in South China and their metallogenic series. Mineralium Deposita, 14(2), 189–194 (in Chinese).

Roda-Robles, E., Keller, P., Pesquera, A., and Fontan, F. (2007) Micas of the muscovite–lepidolite series from Karibib pegmatites, Namibia. Mineralogical Magazine, 71, 41–62.

Rudnick, R.L., and Gao, S. (2003) Composition of the continental crust. Treatise on Geochemistry, 3, 1–64

Sinclair, W.D., Gonevchuk, G.A., Korostelev, P.G., Semenyak, B I., Rodionov, S.M., Seltmann, R., and Stemprok, M. (2014) World Tin and Tungsten Deposit database; Geological Survey of Canada, Open File 7688, 1 .zip file. doi:10.4095/295581

Schaltegger, S., Pettke, T., Audétat, A., Reusser, E., and Heinrich, C.A. (2005) Magmatic-to-hydrothermal crystallization in the W–Sn mineralized Mole Granite (NSW, Australia): Part I: Crystallization of zircon and REE-phosphates over three million years - a geochemical and U–Pb geochronological study. Chemical Geology, 220, 215–235.

Schwinn, G., and Markl, G. (2005) REE systematics in hydrothermal fluorite. Chemical Geology, 216, 225–248.

Simons, B., Andersen, J.C., Shail, R.K., and Jenner, F.E. (2017) Fractionation of Li, Be, Ga, Nb, Ta, In, Sn, Sb, W and Bi in the peraluminous Early Permian Variscan granites of the Cornubian Batholith: precursor processes to magmatic-hydrothermal mineralisation. Lithos, 278, 491–512.

Štemprok, M. (1990) Solubility of tin, tungsten and molybdenum oxides in felsic magmas. Mineralium Deposita, 25, 205–212.

Tang, Y., Cui, K., Zheng, Z., Gao, J., Han, J., Yang, J., and Liu, L. (2020) LA-ICP-MS U-Pb geochronology of wolframite by combining NIST series and common lead-bearing MTM as the primary reference material: Implications for metallogenesis of South China. Gondwana Research, *DOI: 10.1016/j.gr.2020.02.006.*

Taylor, S.R., and Mclennan, S.M. (1985) The continental crust: its composition and evolution, an examination of the geochemical record preserved in sedimentary rocks. Journal of Geology, 94(4), 632–633.

Tischendorf, G., Gottesmann, B., Foerster, H.J., and Trumbull, R.B. (1997) On Li-bearing micas: estimating Li from electron microprobe analyses and an improved diagram for graphical representation. Mineralogical Magazine, 61, 809–834.

Thomas, R., Förster, H., Rickers, K., and Webster, J.D. (2005) Formation of extremely F-rich hydrous melt fractions and hydrothermal fluids during differentiation of highly evolved tin-granite magmas: a melt/fluid-inclusion study. Contributions to Mineralogy and Petrology, 148(5), 582–601.

Vallance, J., Cathelineau, M., Marignac, C., Boiron, M.C., Fourcade, S., Martineau, F., and Fabre, C. (2001) Microfracturing and fluid mixing in granites: W-(Sn) ore deposition at Vaulry (NW French Massif Central). Tectonophysics, 336, 43–61.

Van, Lichtervelde. M., Grégoire, M., Linnen, R.L., Béziat, D., and Salvi, S. (2008) Trace element geochemistry by laser ablation ICP-MS of micas associated with Ta mineralization in the Tanco pegmatite, Manitoba, Canada. Contribution to Mineralogy and Petrology, 155, 791–806.

Vigneresse, J.L. (2006) Element mobility in melts during successive intrusions of crustal-derived magmas and Sn-W mineralization. Resource Geology, 56(3), 293–314.

Vindel, E., Lopez, J.A., Boiron, M.C., Cathelineau, M., and Prieto, A.C. (1995) P-V-T-X-fO_2 evolution from wolframite to sulphide depositional stages in intragranitic W-veins. An example from the Spanish Central System. European Journal of Mineralogist, 7, 675–688.

Wang, F.Y., Li, C.Y., Ling, M.X., Zhang, H., Sun, Y.L., and Sun, W.D. (2011) Geochronology of the Xihuashan Tungsten deposit in Southeastern China: constraints from Re–Os and U–Pb dating. Resource Geology, 61, 414–423.

Wang, L.K., Zhu, W.F., and Zhang, S.L. (1982) On the evolution of two petrogenetic and mineralized series of granites in South China. Geochimica, 4, 329–339 (in Chinese with English abstract).

Wang, R.C., Fontan, F., Chen, X.M., Hu, H., Liu, S.C., and Xu, S.J., (2003) Accessory minerals in the Xihuashan Y-enriched granite complex. The Canadian Mineralogist, 41, 727–748.

Wang, X.L. Qiu, Y., Lu, J.M. Chou, I, Zhang, W.L., Li, G.L, Hu, W.X., Li, Z., and Zhong, R.C. (2020) In situ Raman spectroscopic investigation of the hydrothermal speciation of tungsten: Implications for the ore-forming process. Chemical Geology 532, 119299.

Wei, W.F., Hu, R.Z., Bi, X.W., Peng, J.T., Su, W., Song, S.Q., and Shi, S.H. (2012) Infrared microthermometric and stable isotopic study of fluid inclusions in wolframite at the Xihuashan tungsten deposit, Jiangxi province, China. Mineralium Deposita, 47, 589–605.

Wei, W.F., Hu, R.Z., Peng, J.T., Bi, X.W., Song, S.Q., and Shi, S.H. (2011) Fluid mixing in Xihuashan tungsten deposit, Southern Jiangxi Province: hydrogen and oxygen isotope simulation analysis. Geochimica, 40(1), 45-55 (in Chinese with English abstract).

Wones, D.R., and Eugster, H.R. (1965). Stability of biotite experiment, theory, and application. American Mineralogist, 50, 1228–1272.

Yang, J.H., Peng, J.T., Hu, R.Z., Bi, X.W., Zhao, J.H., Fu, Y.Z., and Shen, N.P. (2013) Garnet geochemistry of tungsten-mineralized Xihuashan granites in South China. Lithos, 177, 79–90.

Yang, J.H., Kang, L.F., Peng, J.T., Zhong, H., Gao, J.F., and Liu, L. (2018) In-situ elemental and isotopic composition of apatite and zircon from the Shuikoushan and

Xihuashan granitic plutons: Implication for Jurassic granitoid-related Cu-Pb-Zn and W mineralization in the Nanling Range, South China. Ore Geology Reviews, 93, 382–403.

Yin, L., Pollard, P., Hu, S.X., and Taylor, R. (1995) Geologic and geochemical characteristics of the Yichun Ta-Nb-Li deposit, Jiangxi Province, South China. Economic Geology, 90, 577–585.

Yin, R., Han, L., Huang, X.L., Li, J., Li, W.X., and Chen, L.L. (2019) Textural and chemical variations of micas as indicators for tungsten mineralization: Evidence from highly evolved granites in the Dahutang tungsten deposit, South China. American Mineralogist, 104, 949–965.

Xie, L., Wang, R.C., Groat, L.A., Zhu, J.C., Huang, F.F., and Cempírek, J. (2015) A combined EMPA and LA-ICP-MS study of Li-bearing mica and Sn–Ti oxide minerals from the Qiguling topaz rhyolite (Qitianling District, China): The role of fluorine in origin of tin mineralization. Ore Geology Reviews, 65, 779–792.

Xie, L., Wang, R.C., Che, X.D., Huang, F.F., Erdmann, S., and Zhang, W.L. (2016) Tracking magmatic and hydrothermal Nb–Ta–W–Sn fractionation using mineral textures and composition: A case study from the late Cretaceous Jiepailing ore district in the Nanling Range in South China. Ore Geology Reviews, 78, 300–321.

Xie, L., Wang, Z., Wang, R., Zhu, J., Che, X., Gao, J., and Zhao, X. (2018) Mineralogical constraints on the genesis of W–Nb–Ta mineralization in the Laiziling granite (Xianghualing district, south China). Ore Geology Reviews, 95, 695–712.

Zhang, C., Holtz, F., Ma, C.Q., Wolff, P.E., and Li, X.Y. (2012) Tracing the evolution and distribution of F and Cl in plutonic system from volatile-bearing minerals: a case study from the Liujiawa pluton (Dabie orogeny, China). Contributions to Mineralogy and Petrology, 164, 859–879.

Zhang, L., Zhuang, L., Qian, Y., Guo, Y., and Qu, P. (1982) Stable isotope geochemistry of granites and tungsten tin deposit in Xihuashan-Piaotang area, Jiangxi Province. In: Hepworth JV, Yu HZ (eds) Symposium on Tungsten geology, Jiangxi, China. ESCAP-RMRDC, Bandung, pp, 553–566.

Zhao, J.H., Zhou, M.F., Yan, D.P., Zheng, J.P., and Li, J.W. (2011) Reappraisal of the ages of Neoproterozoic strata in South China: no connection with the Grenvillian orogeny. Geology, 39, 299–302.

Zhou, X.M., Sun, T., Shen, W.Z., Shu, L.S., and Niu, Y.L. (2006) Petrogenesis of Mesozoic granitoids and volcanic rocks in South China: a response to tectonic evolution. Episodes, 29, 26–33.

Zhu, C., and Sverjensky, D.A. (1992) F-Cl-OH partitioning between biotite and apatite. Geochimica et Cosmochimica Acta, 56, 3435–3467.

FIGURE CAPTIONS

Fig. 1 (a) The distribution of granites and volcanic rocks of different ages in SE China (modified from Li et al. 2010), showing the locations of the Nanling W–Sn polymetallic mineralization region (NPMR) and the Xihuashan tungsten deposit. (b) Simplified geological map of the Xihuashan pluton (modified from Guo et al. 2012), showing four successive intrusions in the Xihuashan mining district (G1–G4, which correspond to coarse-grained biotite granite, medium-grained biotite granite, medium- to fine-grained biotite granite, and fine-grained biotite granite, respectively. After Wang et al. 2003).

Fig. 2 Hand specimen photographs (left) and photomicrographs (right) showing the petrography of the Xihuashan granites and greisen (in cross-polarized light) and the different micas encountered in this study. (a) Biotite granite. Biotite (siderophyllite) and associated apatite and ilmenite inclusions. (b) Two-mica granite. Biotite (lithian siderophyllite), muscovite and associated apatite and ilmenite inclusions; the rim of the biotite was eroded, as shown by the irregular embayed form. (c) Muscovite granite. Muscovite is present between the feldspar (both plagioclase and K-feldspar) and quartz. (d) Greisen. Biotite (lithian siderophyllite) and Li-mica occur between quartz grains. Mineral abbreviations: K-feldspar (Kfs), plagioclase (Pl), quartz (Qtz), biotite (Bt), muscovite (Ms), apatite (Ap), ilmenite (Ilm), zircon (Zrn), xenotime (Xtm).

Fig. 3 The diagrams of (a) TAS, (b) A/NK vs. A/CNK, and (c–h) TiO_2, MgO, P_2O_5, F, K_2O, and CaO contents versus Fe_2O_3 for the Xihuashan pluton. The total Fe in the whole rock analyses is reported as Fe_2O_3. Plots I–IV from Guo et al. (2012) represent the data of different intrusions.

Fig. 4 Chondrite-normalized REE patterns and mean upper crust-normalized multi-element diagrams for rocks in the Xihuashan pluton. The chondrite and mean upper crust values are from Taylor and McLennan (1985) and Rudnick and Gao (2003), respectively. Data in shaded field are from Guo et al. (2012).

Fig. 5 (a-d) Back-scattered-electron (BSE) images of micas in different intrusions of the Xihuashan pluton; (e) and (f) representative BSE images of wolframite in greisen.

Fig. 6 Diagrams of TiO_2, Al_2O_3, FeO^{Tot}, MgO, F, and Cl contents versus SiO_2 for micas in the rocks of the Xihuashan pluton. BG = biotite granite, TMG = two-mica granite, and MG = muscovite granite.

Fig. 7 Diagrams of V, Cs, Rb, Nb, Ta, W, Sn, and Nb/Ta versus FeO^{Tot} + MnO + MgO contents for micas in the rocks of the Xihuashan pluton. The dashed lines connect the cores and corresponding rims of zoned mica. BG = biotite granite, TMG = two-mica granite, and MG = muscovite granite.

Fig. 8 (a) Representative BSE image, (b) Raman spectra, (c) chondrite-normalized REE patterns, and (d) mean upper crust-normalized multi-element diagrams for siderite in the Xihuashan muscovite granite and greisen. Chondrite and mean upper crust values are from Taylor and McLennan (1985) and Rudnick and Gao (2003), respectively.

Fig. 9 (a, b) Variation of measured Li_2O versus SiO_2 and F for micas in the rocks of the Xihuashan pluton. The regression equations of (1) $Li_2O = 0.289 \times SiO_2 - 9.658$ and (2) $Li_2O = 0.3935 \times F^{1.326}$ from Tischendorf et al. (1997) can be applied to trioctahedral and dioctahedral micas, respectively. (c) Relationships between measured Li_2O and F in hydrothermal micas, which define a regression equation of (3) $Li_2O = 0.0748 \times F^2 + 0.0893 \times F$ that could be applied to the hydrothermal micas in our samples. (d) Comparison between measured and calculated Li_2O for micas in the rocks of the Xihuashan pluton. Some data for the hydrothermal micas were taken from previous studies (Van Lichtervelde 2008; Akoh and Ogunleye 2014; Xie et al. 2015; Yin et al. 2019; Ma et al. 2020). BG = biotite granite, TMG = two-mica granite, and MG = muscovite granite.

Fig. 10 (a) Variations in the compositions of mica from the Xihuashan pluton on the diagram of [Mg – Li] vs. [Fe^{Tot} + Mn + Ti – Al^{VI}] (according to Tischendorf et al. 1997). (b) Relationships between Li and octahedral cations (based on Foster 1960). The arrows indicate the trends in mica compositions due to magmatic evolution. The shadow area represents the field of the transitional series, known as the ferrous aluminous micas (Monier and Robert 1986). D.T. and T.T. denote the compositional trends of dioctahedral and trioctahedral micas, respectively. BG = biotite granite, TMG = two-mica granite, and MG = muscovite granite.

Fig. 11 Plots of (a) SiO_2 versus log(fH_2O/fHF), (b) Fe^{3+}/Fe^{2+} versus log(fH_2O/fHF), and (c) SiO_2 versus W_F^m for micas in the Xihuashan pluton. BG = biotite granite, TMG = two-mica granite, and MG = muscovite granite.

Fig. 12 Plots of Rb, Cs, and W versus K/Rb for micas in the Xihuashan pluton. BG = biotite granite, TMG = two-mica granite, and MG = muscovite granite.

Fig. 13 Cartoon of tungsten mineralization in the Xihuashan pluton, illustrating the relationship between the evolution of the magmatic–hydrothermal system and the W mineralization. The spatial relationships between the bodies of granite and greisen are based on previous investigations (Liu 2005; Huang et al. 2006).

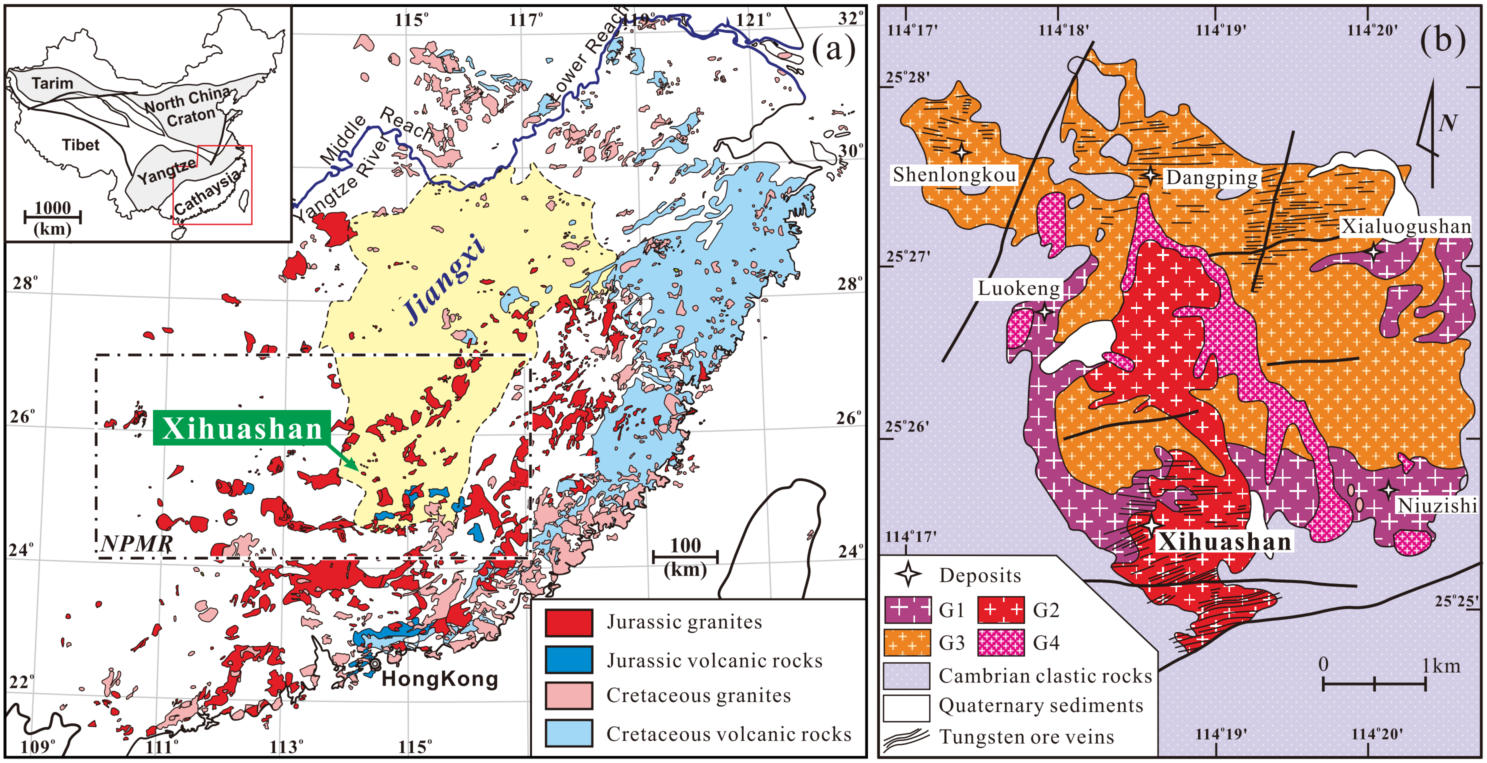
(a)
Tarim
North China Craton
Tibet
Yangtze
Cathaysia
1000 (km)
115°
117°
119°
121°
32°
30°
28°
26°
24°
22°
109°
111°
113°
Middle Reach
Yangtze River
Lower Reach
Jiangxi
Xihuashan
NPMR
100 (km)
HongKong
Jurassic granites
Jurassic volcanic rocks
Cretaceous granites
Cretaceous volcanic rocks
(b)
114°17'
114°18'
114°19'
114°20'
25°28'
25°27'
25°26'
25°25'
N
Shenlongkou
Dangping
Xialuogushan
Luokeng
Niuzishi
Xihuashan
Deposits
G1
G2
G3
G4
Cambrian clastic rocks
Quaternary sediments
Tungsten ore veins
0
1km

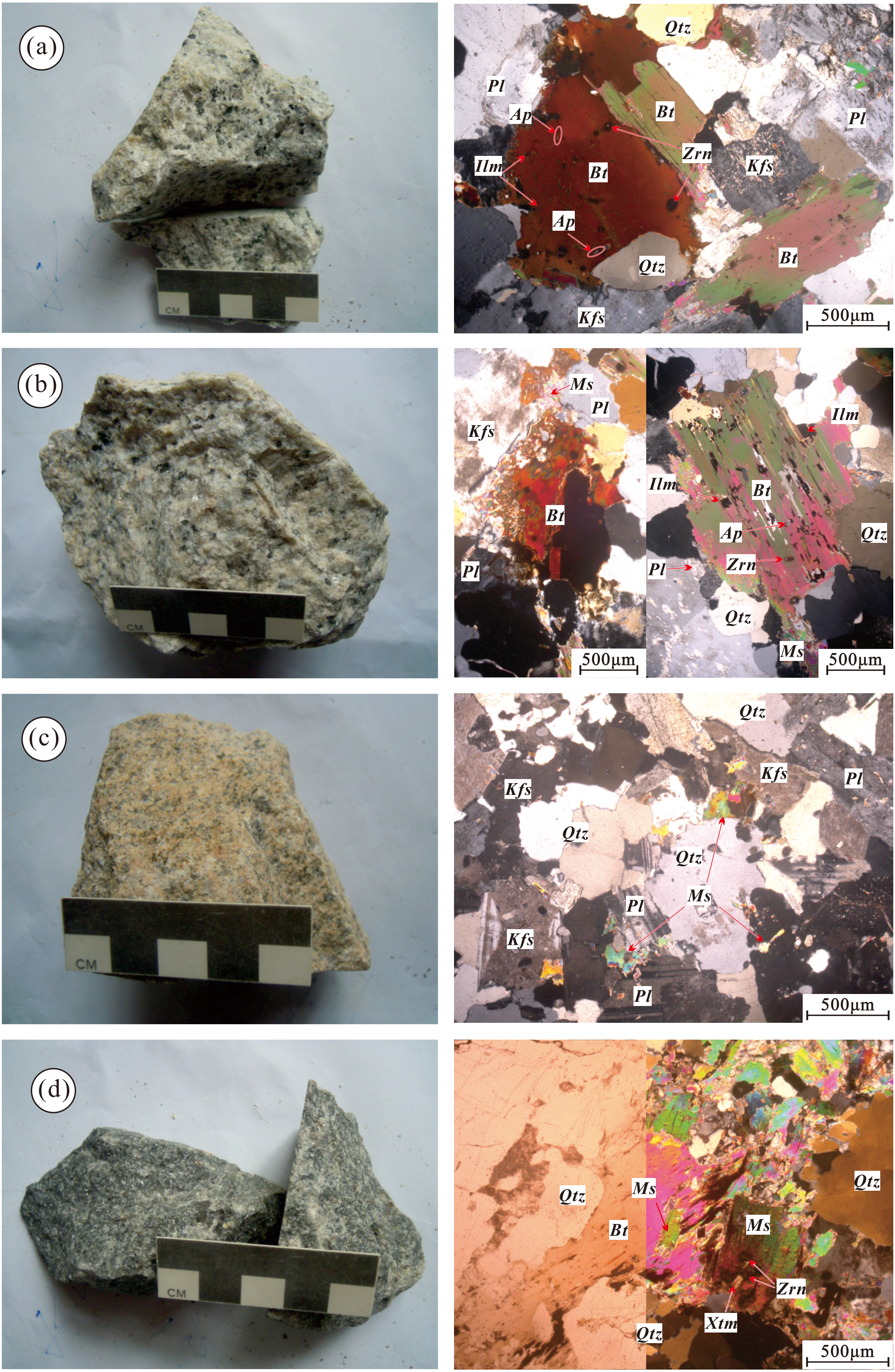
(a)
CM
Qtz
Pl
Ap
Bt
Ilm
Zrn
Bt
Pl
Kfs
Ap
Qtz
Bt
Kfs
500μm
(b)
CM
Ms
Pl
Kfs
Bt
Pl
500μm
Ilm
Ilm
Bt
Ap
Qtz
Pl
Zrn
Qtz
Ms
500μm
(c)
CM
Qtz
Kfs
Kfs
Pl
Qtz
Qtz
Ms
Pl
Kfs
Pl
500μm
(d)
CM
Qtz
Bt
Ms
Ms
Qtz
Zrn
Xtm
Qtz
500μm

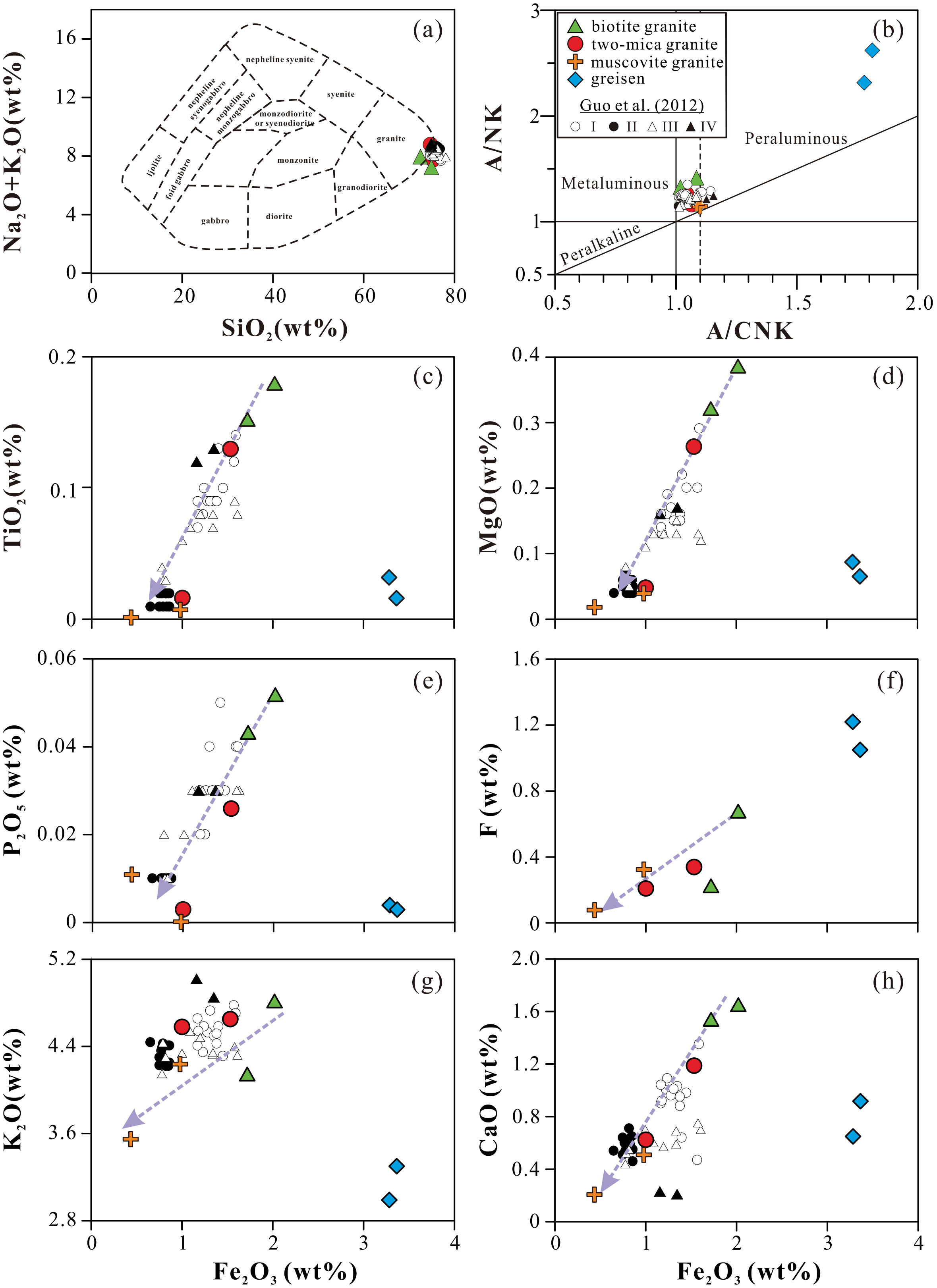
(a)
nepheline syenite
nepheline syenogabbro
nepheline monzogabbro
syenite
monzodiorite or syenodiorite
granite
monzonite
ijolite
foid gabbro
granodiorite
gabbro
diorite
Na_2O+K_2O(wt%)
SiO_2(wt%)
0
4
8
12
16
0
20
40
60
80
(b)
biotite granite
two-mica granite
muscovite granite
greisen
Guo et al. (2012)
○ I ● II △ III ▲ IV
Peraluminous
Metaluminous
Peralkaline
A/NK
A/CNK
0.5
1
2
3
0.5
1.0
1.5
2.0
(c)
TiO_2(wt%)
0
0.1
0.2
(d)
MgO(wt%)
0
0.1
0.2
0.3
0.4
(e)
P_2O_5 (wt%)
0
0.02
0.04
0.06
(f)
F (wt%)
0
0.4
0.8
1.2
1.6
(g)
K_2O(wt%)
2.8
3.6
4.4
5.2
Fe_2O_3 (wt%)
0
1
2
3
4
(h)
CaO (wt%)
0
0.4
0.8
1.2
1.6
2.0
Fe_2O_3 (wt%)
0
1
2
3
4

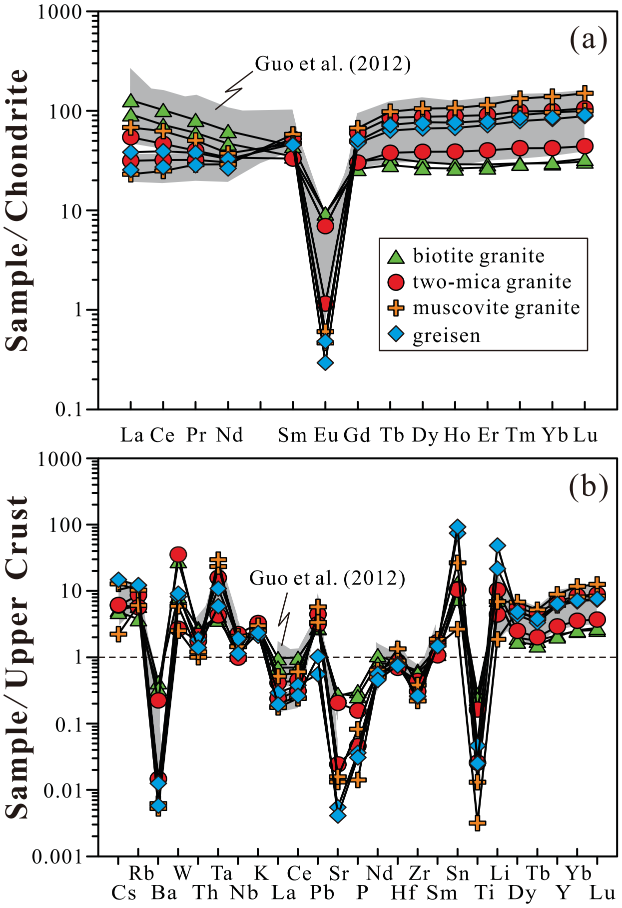
(a)
Guo et al. (2012)
Sample/Chondrite
1000
100
10
1
0.1
biotite granite
two-mica granite
muscovite granite
greisen
La Ce Pr Nd Sm Eu Gd Tb Dy Ho Er Tm Yb Lu
(b)
Guo et al. (2012)
Sample/Upper Crust
1000
100
10
1
0.1
0.01
0.001
Rb W Ta K Ce Sr Nd Zr Sn Li Tb Yb
Cs Ba Th Nb La Pb P Hf Sm Ti Dy Y Lu

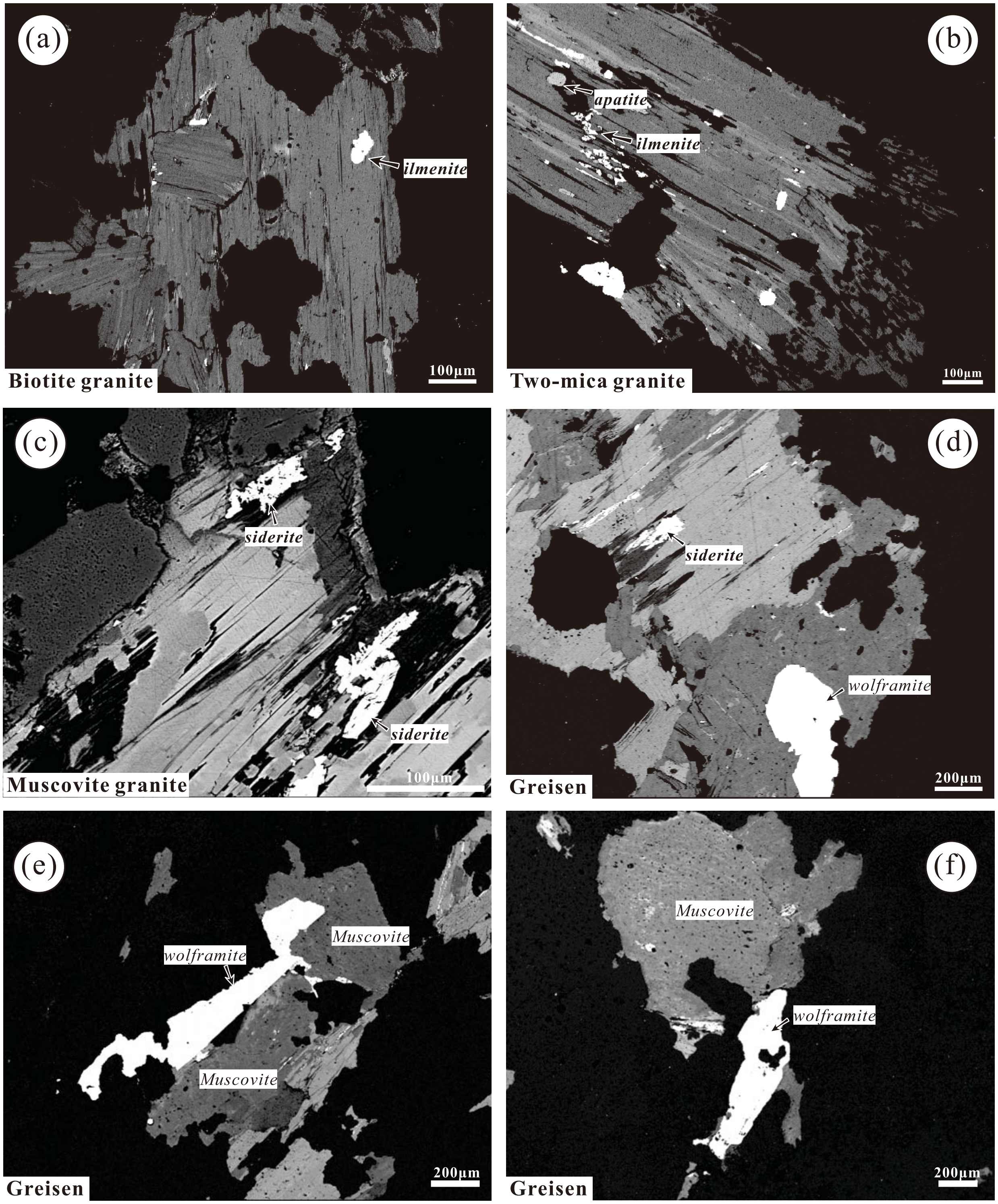
(a)
ilmenite
Biotite granite
100μm
(b)
apatite
ilmenite
Two-mica granite
100μm
(c)
siderite
siderite
Muscovite granite
100μm
(d)
siderite
wolframite
Greisen
200μm
(e)
wolframite
Muscovite
Muscovite
Greisen
200μm
(f)
Muscovite
wolframite
Greisen
200μm

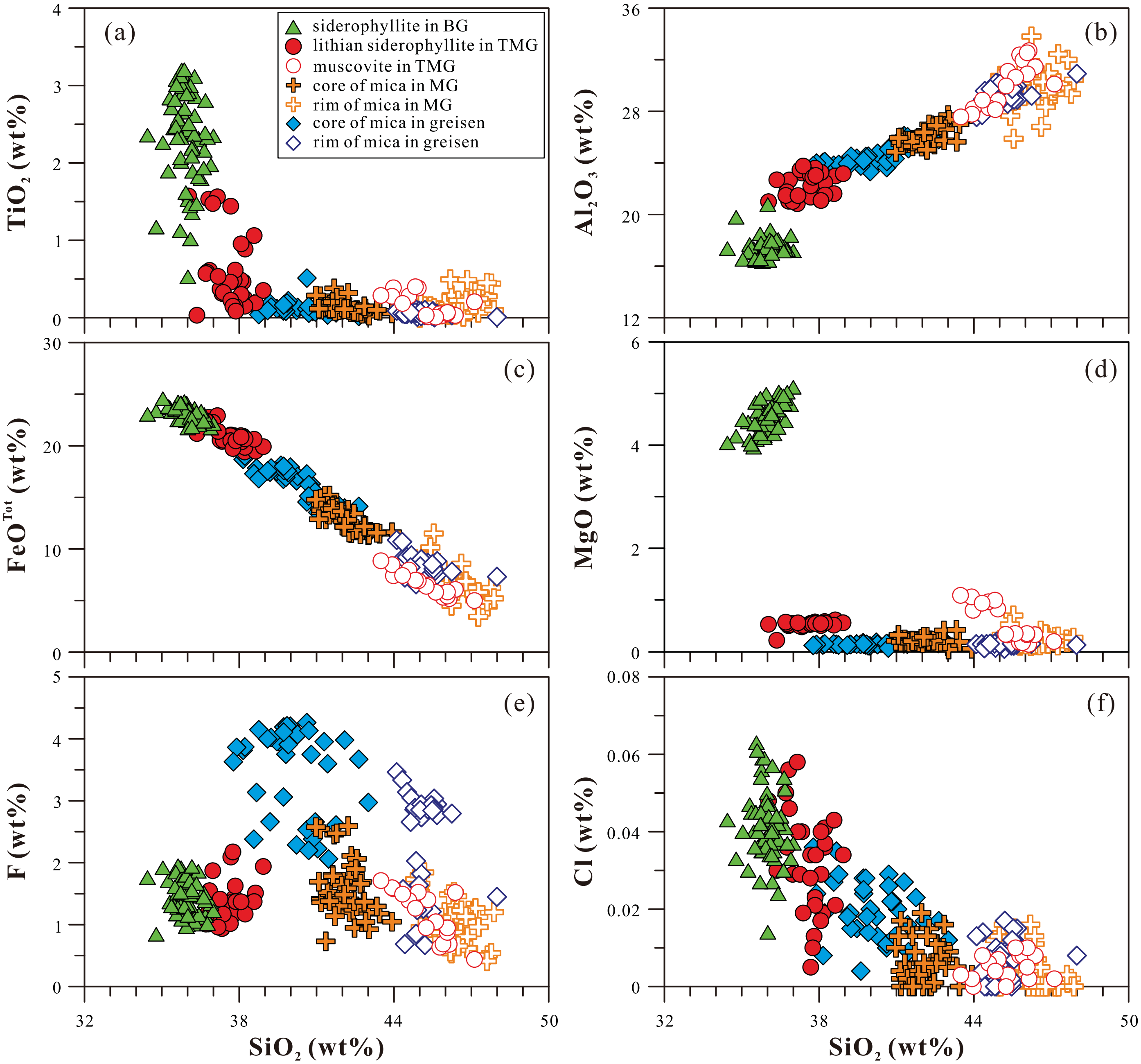

(a)
(b)
(c)
(d)
(e)
(f)
siderophyllite in BG
lithian siderophyllite in TMG
muscovite in TMG
core of mica in MG
rim of mica in MG
core of mica in greisen
rim of mica in greisen
TiO_2 (wt%)
Al_2O_3 (wt%)
FeO^{Tot} (wt%)
MgO (wt%)
F (wt%)
Cl (wt%)
SiO_2 (wt%)
SiO_2 (wt%)
0
1
2
3
4
12
20
28
36
0
10
20
30
0
2
4
6
0
1
2
3
4
5
0
0.02
0.04
0.06
0.08
32
38
44
50
32
38
44
50

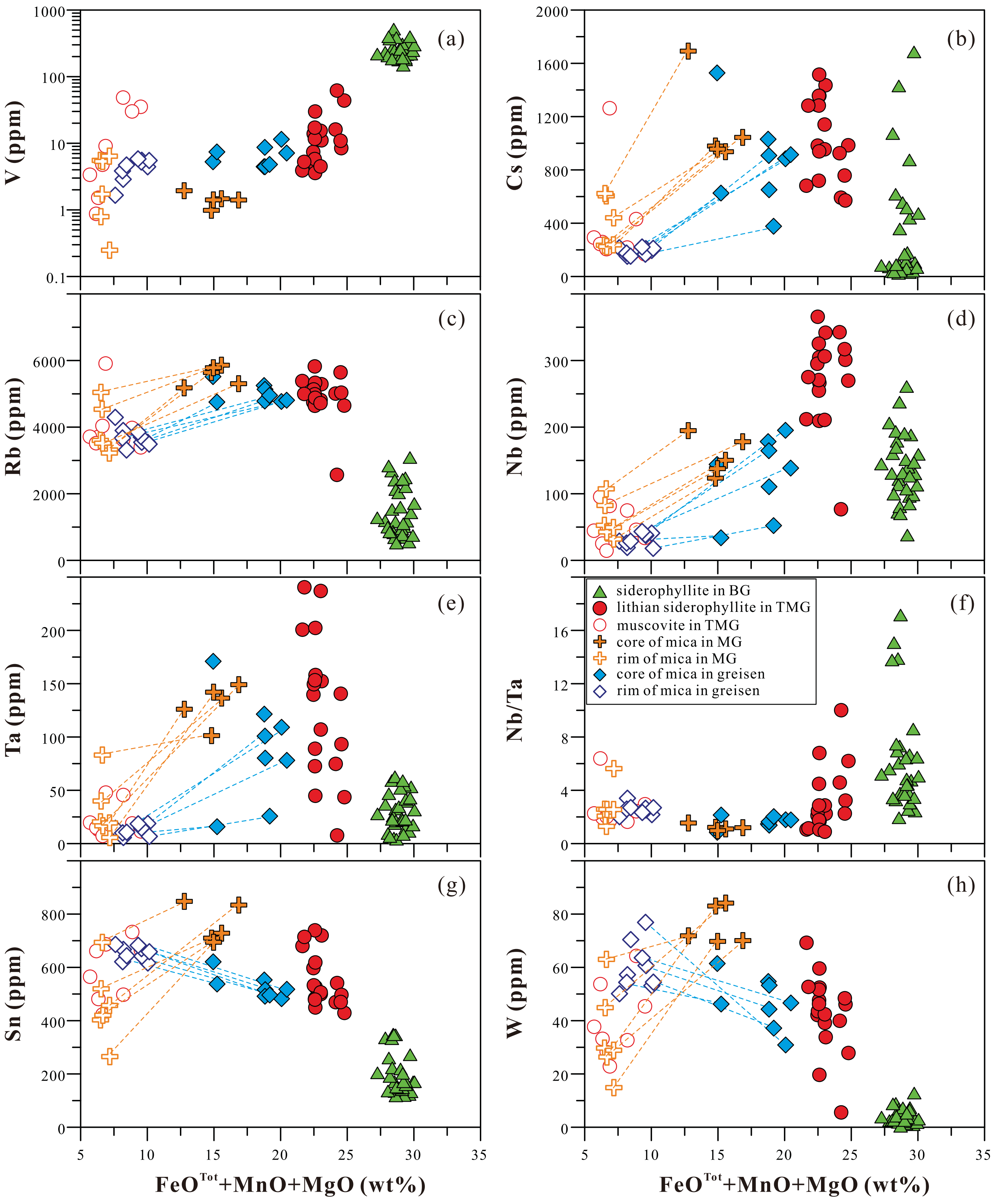
(a)
(b)
(c)
(d)
(e)
(f)
(g)
(h)
V (ppm)
Cs (ppm)
Rb (ppm)
Nb (ppm)
Ta (ppm)
Nb/Ta
Sn (ppm)
W (ppm)
1000
100
10
1
0.1
2000
1600
1200
800
400
0
6000
4000
2000
0
300
200
100
0
200
150
100
50
0
16
12
8
4
0
800
600
400
200
0
80
60
40
20
0
5
10
15
20
25
30
35
siderophyllite in BG
lithian siderophyllite in TMG
muscovite in TMG
core of mica in MG
rim of mica in MG
core of mica in greisen
rim of mica in greisen
FeO^{Tot}+MnO+MgO (wt%)
FeO^{Tot}+MnO+MgO (wt%)

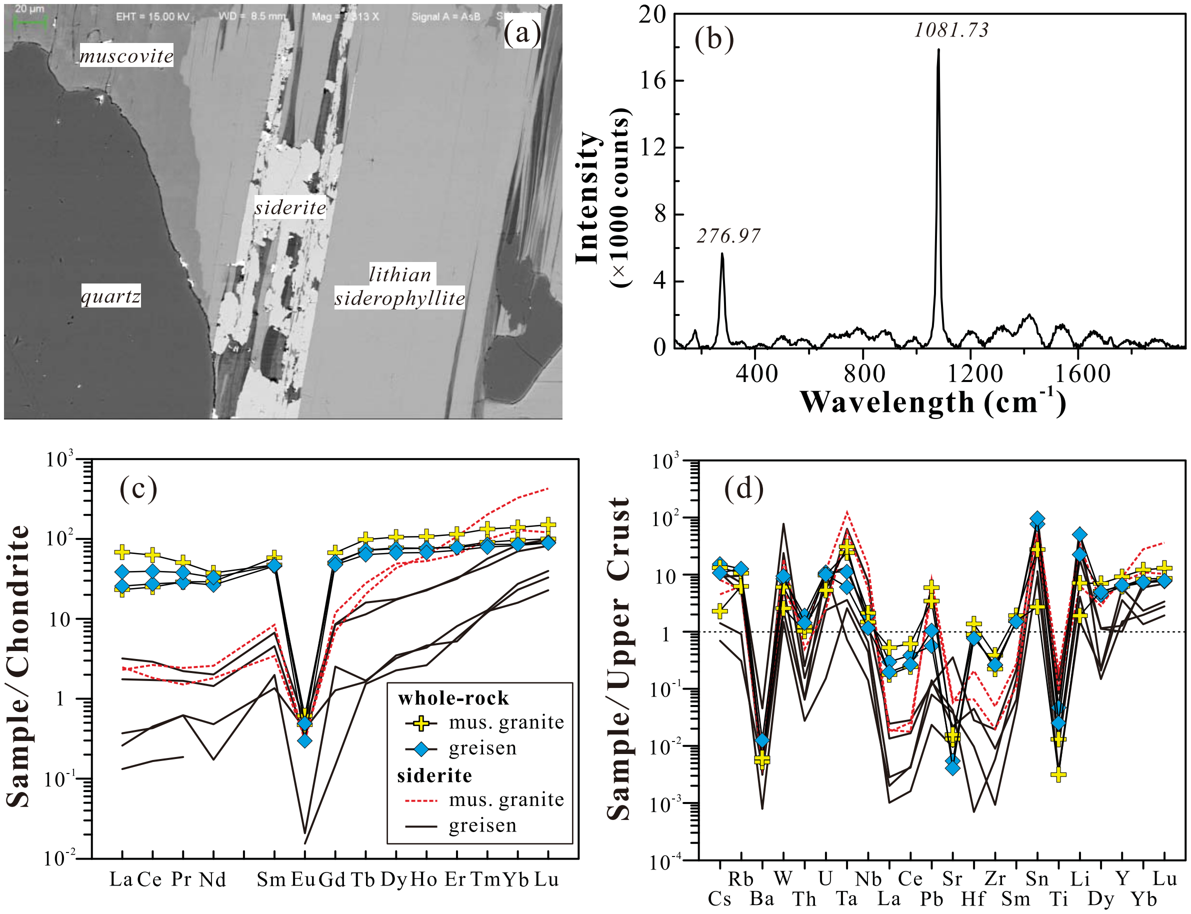
(a)
20 μm
EHT = 15.00 kV
WD = 8.5 mm
Signal A = AsB
muscovite
siderite
quartz
lithian siderophyllite
(b)
1081.73
276.97
Intensity (×1000 counts)
Wavelength (cm-1)
0
4
8
12
16
20
400
800
1200
1600
(c)
Sample/Chondrite
10-2
10-1
1
10
102
103
La Ce Pr Nd Sm Eu Gd Tb Dy Ho Er Tm Yb Lu
whole-rock
mus. granite
greisen
siderite
mus. granite
greisen
(d)
Sample/Upper Crust
10-4
10-3
10-2
10-1
1
10
102
103
Cs Rb Ba W Th U Ta Nb La Ce Pb Sr Hf Zr Sm Sn Ti Li Dy Y Yb Lu

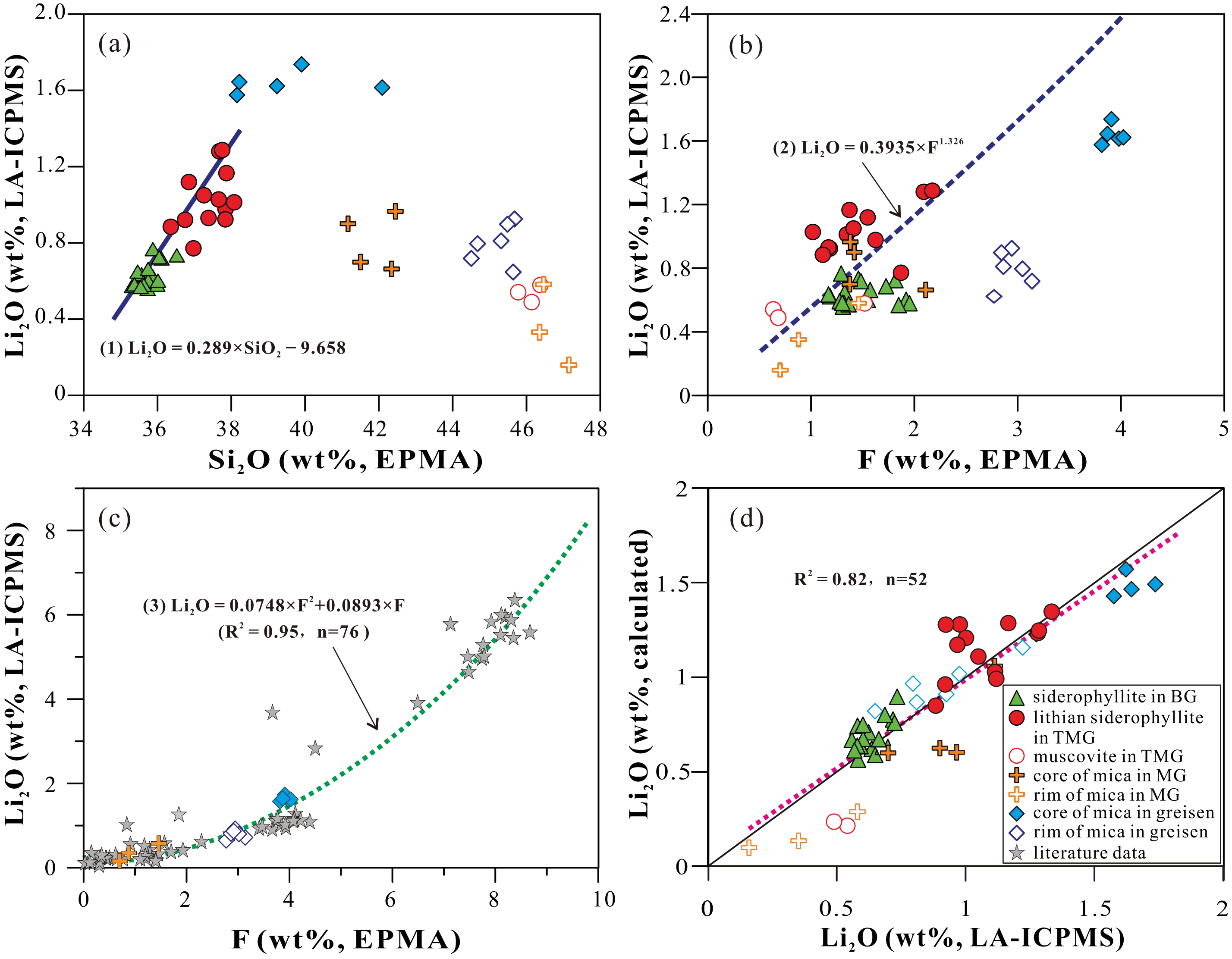

(a)
Li_2O (wt%, LA-ICPMS)
Si_2O (wt%, EPMA)
(1) $Li_2O = 0.289×SiO_2 − 9.658$
0
0.4
0.8
1.2
1.6
2.0
34
36
38
40
42
44
46
48
(b)
Li_2O (wt%, LA-ICPMS)
F (wt%, EPMA)
(2) $Li_2O = 0.3935×F^{1.326}$
0
0.4
0.8
1.2
1.6
2.0
2.4
0
1
2
3
4
5
(c)
Li_2O (wt%, LA-ICPMS)
F (wt%, EPMA)
(3) $Li_2O = 0.0748×F^2+0.0893×F$
($R^2 = 0.95$, n=76)
0
2
4
6
8
0
2
4
6
8
10
(d)
Li_2O (wt%, calculated)
Li_2O (wt%, LA-ICPMS)
$R^2 = 0.82$, n=52
0
0.5
1
1.5
2
0
0.5
1
1.5
2
▲ siderophyllite in BG
● lithian siderophyllite in TMG
○ muscovite in TMG
✚ core of mica in MG
✚ rim of mica in MG
◆ core of mica in greisen
◇ rim of mica in greisen
★ literature data

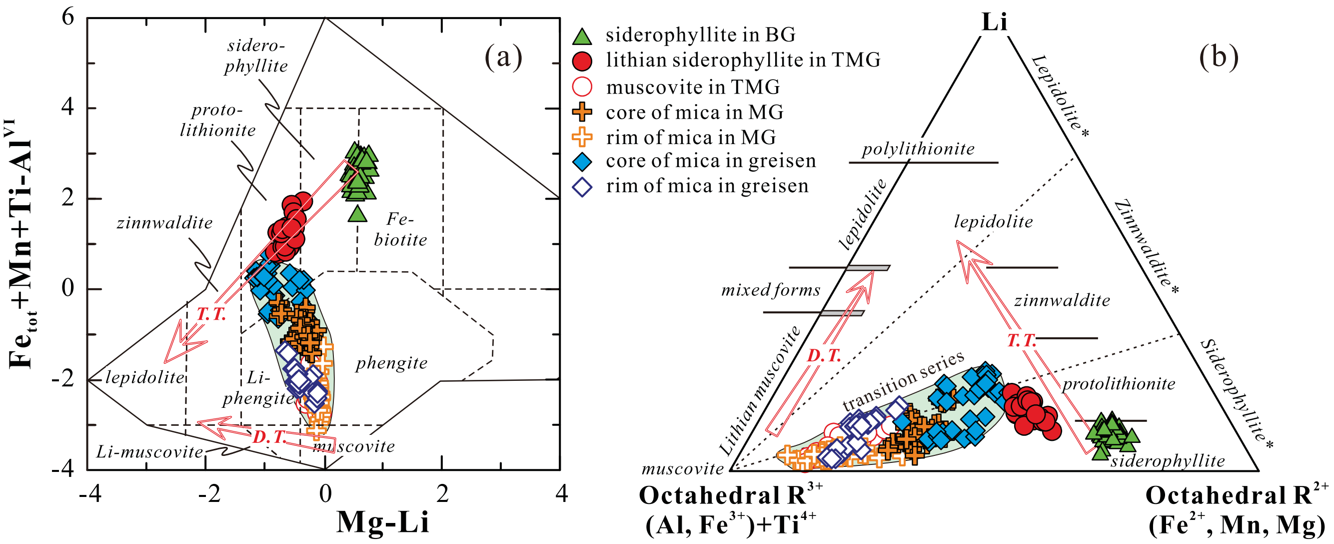
(a)
(b)
siderophyllite in BG
lithian siderophyllite in TMG
muscovite in TMG
core of mica in MG
rim of mica in MG
core of mica in greisen
rim of mica in greisen
sidero-phyllite
proto-lithionite
zinnwaldite
lepidolite
Li-phengite
Li-muscovite
muscovite
phengite
Fe-biotite
T. T.
D. T.
Fe_{tot}+Mn+Ti-Al^{VI}
Mg-Li
6
4
2
0
-2
-4
-4
-2
0
2
4
Li
Lepidolite*
Zinnwaldite*
Siderophyllite*
polylithionite
lepidolite
mixed forms
Lithian muscovite
transition series
protolithionite
siderophyllite
muscovite
Octahedral R^{3+} (Al, Fe^{3+})+Ti^{4+}
Octahedral R^{2+} (Fe^{2+}, Mn, Mg)

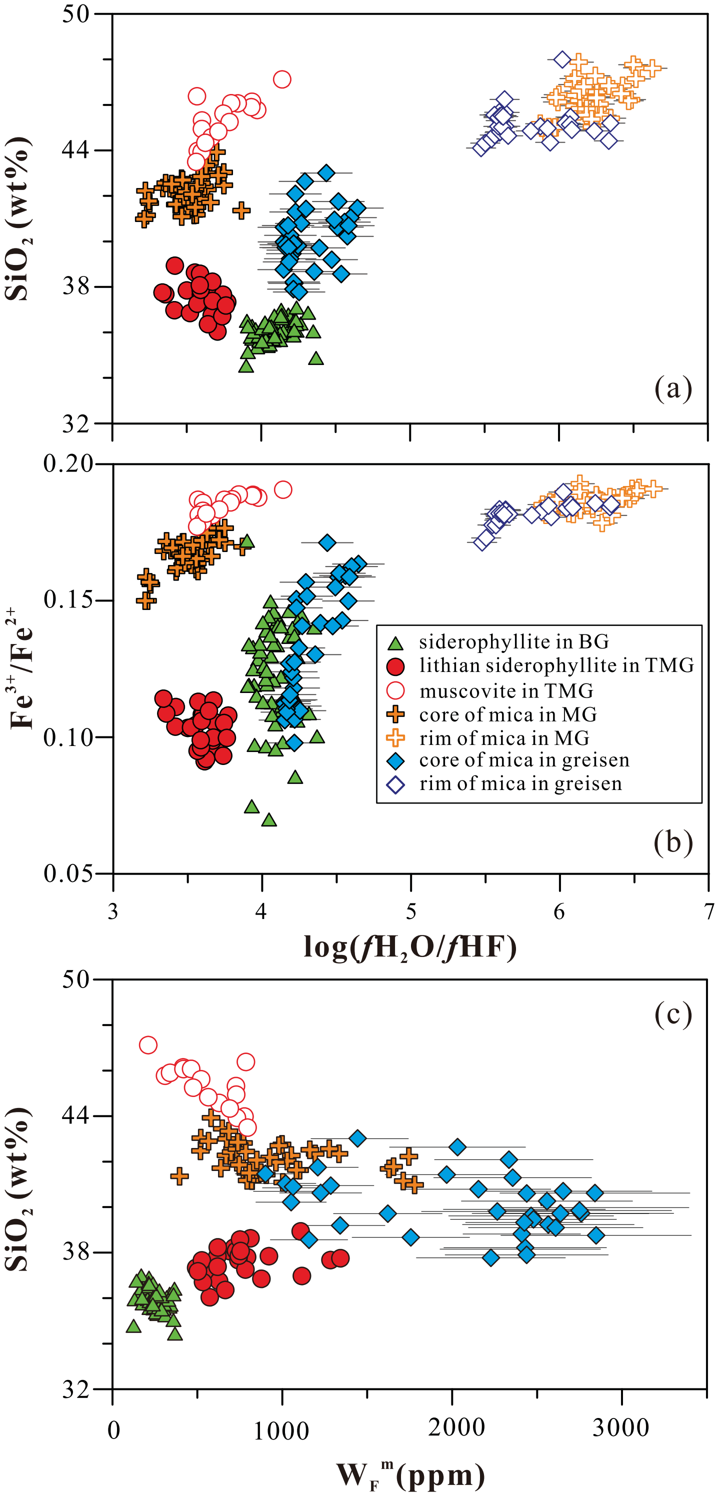
50
44
38
32
SiO₂ (wt%)
(a)
0.20
0.15
0.10
0.05
Fe³⁺/Fe²⁺
siderophyllite in BG
lithian siderophyllite in TMG
muscovite in TMG
core of mica in MG
rim of mica in MG
core of mica in greisen
rim of mica in greisen
(b)
3
4
5
6
7
log(fH₂O/fHF)
50
44
38
32
SiO₂ (wt%)
(c)
0
1000
2000
3000
W_F^m(ppm)

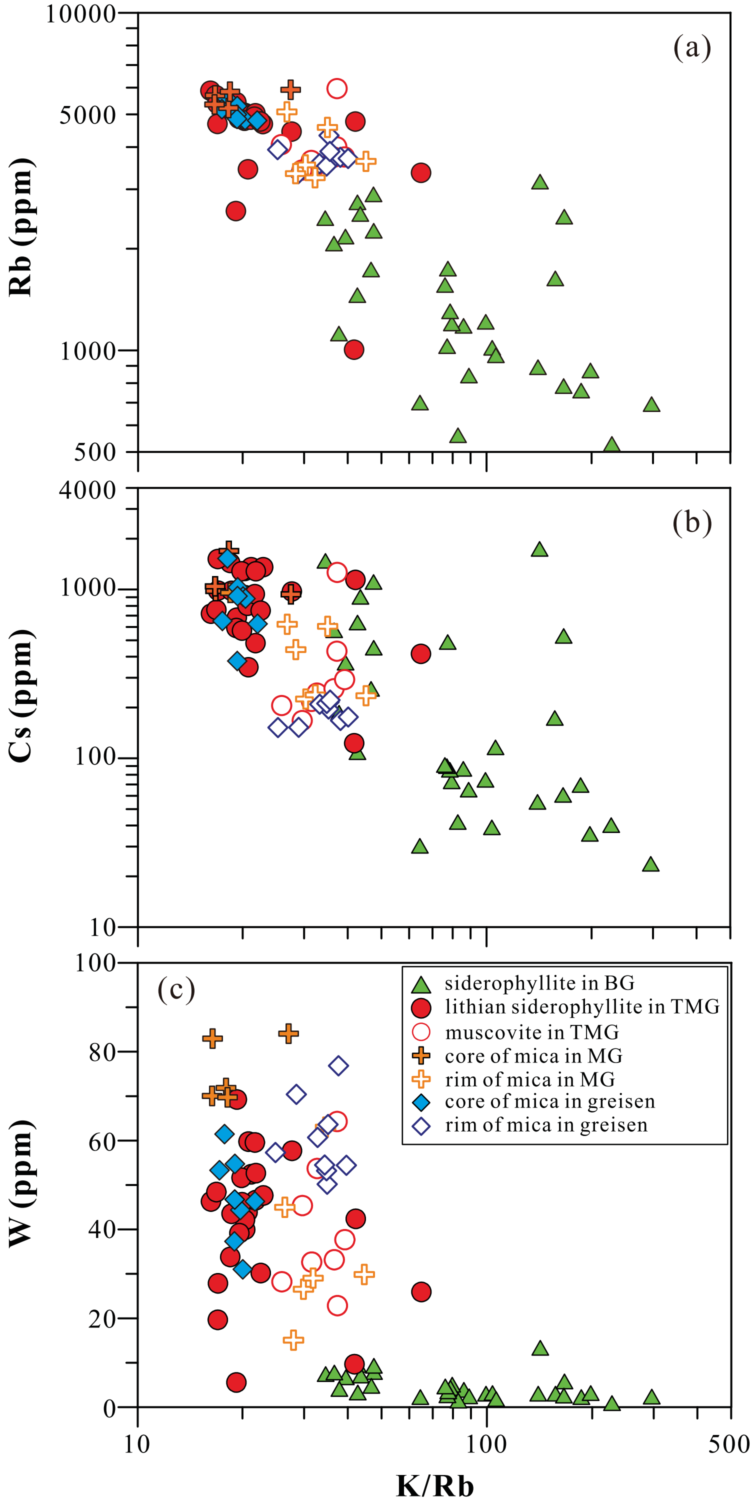

(a)
Rb (ppm)
10000
5000
1000
500
(b)
Cs (ppm)
4000
1000
100
10
(c)
W (ppm)
100
80
60
40
20
0
10
100
500
K/Rb
siderophyllite in BG
lithian siderophyllite in TMG
muscovite in TMG
core of mica in MG
rim of mica in MG
core of mica in greisen
rim of mica in greisen

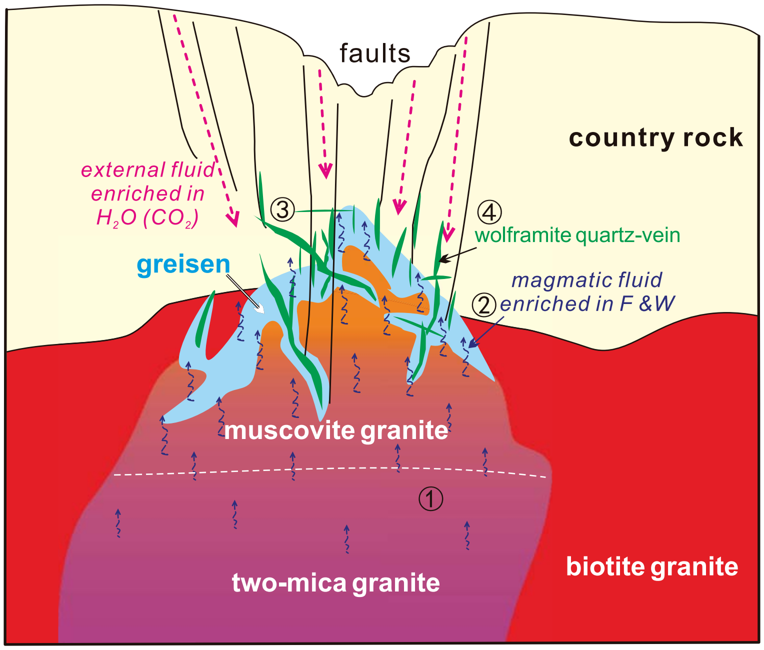
faults
country rock
external fluid enriched in H2O (CO2)
③
④
wolframite quartz-vein
greisen
magmatic fluid
② enriched in F &W
muscovite granite
①
two-mica granite
biotite granite